

UWThPh-1996-66
 HEPHY-PUB 663/97
 DESY 97-003
 hep-ph/9701336

Search of Stop, Sbottom, τ -Sneutrino, and Stau at an e^+e^- Linear Collider with $\sqrt{s} = 0.5 - 2$ TeV

A. Bartl^{*1}, H. Eberl^{†2}, S. Kraml^{‡2},
 W. Majerotto^{♭2}, W. Porod^{‡1}, A. Sopczak^{‡3}

(1) *Institut für Theoretische Physik, Universität Wien, A-1090 Vienna, Austria*

(2) *Institut für Hochenergiephysik, Österreichische Akademie der Wissenschaften,
 A-1050 Vienna, Austria*

(3) *DESY-Zeuthen, D-15738 Zeuthen, Germany*

Abstract

We discuss pair production and decays of stops, sbottoms, τ -sneutrinos, and staus in e^+e^- annihilation in the energy range $\sqrt{s} = 500$ GeV to 2 TeV. Numerical predictions within the Minimal Supersymmetric Standard Model (MSSM) for cross sections and decay rates are presented. We study the stop discovery potential for $\sqrt{s} = 500$ GeV and 10 fb^{-1} integrated luminosity for polarized e^- beams. Moreover, we give an estimate of the error of the soft-breaking stop and sbottom parameters that can be obtained by cross section measurements with polarized e^- beams.

^{*} bartl@Pap.UniVie.ac.at, [†] helmut@qhepu1.oeaw.ac.at, [‡] kraml@hephy.oeaw.ac.at,
[♭] majer@qhepu1.oeaw.ac.at, [‡] porod@Pap.UniVie.ac.at, [‡] andre.sopczak@cern.ch;
<http://wwwhephy.oeaw.ac.at/p3w/theory/susy/>

1 Introduction

If nature is supersymmetric at the weak interaction scale, the masses of the supersymmetric (SUSY) particles are expected to be lower than approximately 1 TeV [1, 2]. The weakly interacting SUSY particles are then within the reach of an e^+e^- linear collider with a center-of-mass energy between 500 GeV and 2 TeV. An e^+e^- linear collider in this energy range will not only be a discovery machine for SUSY particles [3, 4, 5], but will also allow detailed measurements of the underlying SUSY parameters [6]. The experimental search of SUSY particles which are relatively light will be particularly important. The lighter scalar top quark \tilde{t}_1 , the SUSY partner of the top quark, and for $\tan\beta \gtrsim 10$ also the sbottom \tilde{b}_1 or the stau $\tilde{\tau}_1$ may even be the lightest visible SUSY particle [7, 8, 9, 10]. The reason is that the Yukawa interactions reduce the soft SUSY breaking masses of the left and right sfermions, \tilde{f}_L and \tilde{f}_R , of the 3^{rd} generation, compared to those of the 1^{st} and 2^{nd} generation [11, 12], and also induce a mixing which may make one mass-eigenstate rather light. The production cross sections and the decay rates, and thus the discovery reach of these sfermions show a distinct dependence on the \tilde{f}_L - \tilde{f}_R mixing angles [4, 13]. If the gluino is heavier than \tilde{t}_1 and \tilde{b}_1 the most important decay modes of these squarks are those into quarks and neutralinos or charginos.

We present results for the production of stops, sbottoms, τ -sneutrinos, and staus in e^+e^- annihilation at energies between $\sqrt{s} = 500$ GeV and 2 TeV. We also discuss in detail the decays of these particles. Furthermore, we present an example for signal selection and background rejection for stop production at $\sqrt{s} = 500$ GeV and $\mathcal{L} = 10 \text{ fb}^{-1}$. In addition, we investigate the possibility of determining the masses and mixing angle of stops. If SUSY particles are experimentally discovered, the measurement of their properties will be the most important step further. Polarization of the e^- beam plays an important rôle. As we will show, from measurements of the production cross sections with polarized e^- beams we can determine the masses and mixing angles of the stops and sbottoms and in turn the underlying soft SUSY breaking parameters with good precision. Knowing the latter we will be able to test the theoretical hypotheses about the SUSY breaking mechanism.

We perform our calculations in the framework of the Minimal Supersymmetric Standard Model (MSSM) [1, 2]. This contains the Standard Model (SM) particles, sleptons $\tilde{\ell}^\pm$, sneutrinos $\tilde{\nu}_\ell$, squarks \tilde{q} , gluinos \tilde{g} , two pairs of charginos $\tilde{\chi}_i^\pm$, $i = 1, 2$, four neutralinos $\tilde{\chi}_k^0$, $k = 1, \dots, 4$, and five Higgs particles h^0 , H^0 , A^0 , H^\pm [1, 2, 14]. The phenomenology of stops, sbottoms, staus, and τ -sneutrinos, and their decay products is determined by the following parameters:

- the soft-breaking parameters $M_{\tilde{L}}$, $M_{\tilde{E}}$, $M_{\tilde{Q}}$, $M_{\tilde{U}}$, $M_{\tilde{D}}$, A_τ , A_t , A_b , which determine the mass matrices of the stau, stop, and sbottom systems, and the mass of the τ -sneutrino,
- the (soft-breaking) $SU(2)$ and $U(1)$ gaugino masses M and M' ,

- the higgsino mass parameter μ , and $\tan \beta = v_2/v_1$ (where v_1 and v_2 are the vacuum expectation values of the neutral members of the two Higgs doublets).

We assume the GUT relations $M'/M = \frac{5}{3} \tan^2 \Theta_W \approx 0.5$, and $m_{\tilde{g}}/M = \alpha_s/\alpha_2 \approx 3$, where $m_{\tilde{g}}$ is the gluino mass. Furthermore, we assume that the $\tilde{\chi}_1^0$ is the lightest SUSY particle (LSP).

The lower model independent mass bound for stops obtained at LEP1 is 45 GeV [15]. Stronger limits up to 65 GeV are reported from the data taking at LEP1.5 at 130–161 GeV [16]. The $D\bar{0}$ experiment at the TEVATRON excludes the mass range $40 \text{ GeV} \lesssim m_{\tilde{t}} \lesssim 100 \text{ GeV}$ for the stop, if the mass difference $m_{\tilde{t}} - m_{\tilde{\chi}_1^0} \gtrsim 30 \text{ GeV}$ [17].

In Section 2 we shortly review the basic facts about L–R mixing of stops, sbottoms, and staus. We also present numerical results for the production cross sections of stops, sbottoms, τ -sneutrinos, and staus for unpolarized and polarized e^- beams. In Section 3 we describe the decays of stops, sbottoms, τ -sneutrinos, and staus and present numerical results for the most important branching ratios. We also list the signatures which are expected to be relevant at $\sqrt{s} = 500 \text{ GeV}$. In Section 4 we describe an event generator for $\tilde{t}_1 \bar{\tilde{t}}_1$ production and decay. In Section 5 experimental sensitivities are determined based on Monte Carlo simulations. In Section 6 we give an estimate of the experimental error to be expected for stop and sbottom masses and the stop mixing angle, as well as for the soft SUSY breaking parameters. Section 7 gives a summary.

2 Cross Sections for Pair Production of Stops, Sbottoms, τ -Sneutrinos, and Staus

2.1 Left-Right Sfermion Mixing

The SUSY partners of the SM fermions with left and right helicity are the left and right sfermions. In the case of stop, sbottom, and stau the left and right states are in general mixed. In the $(\tilde{f}_L, \tilde{f}_R)$ basis the mass matrix is [7, 14]

$$M_f^2 = \begin{pmatrix} m_{\tilde{f}_L}^2 & a_f m_f \\ a_f m_f & m_{\tilde{f}_R}^2 \end{pmatrix} \quad (1)$$

with

$$m_{\tilde{f}_L}^2 = M_{\tilde{F}}^2 + m_Z^2 \cos 2\beta (T_f^3 - e_f \sin^2 \theta_W) + m_f^2, \quad (2)$$

$$m_{\tilde{f}_R}^2 = M_{\tilde{F}'}^2 + e_f m_Z^2 \cos 2\beta \sin^2 \theta_W + m_f^2, \quad (3)$$

$$a_t \equiv A_t - \mu \cot \beta, \quad a_b \equiv A_b - \mu \tan \beta, \quad a_\tau \equiv A_\tau - \mu \tan \beta, \quad (4)$$

where e_f and T_f^3 are the charge and the third component of the weak isospin of the sfermion \tilde{f} , $M_{\tilde{F}} = M_{\tilde{Q}}$ for $\tilde{f}_L = \tilde{t}_L, \tilde{b}_L$, $M_{\tilde{F}} = M_{\tilde{L}}$ for $\tilde{f}_L = \tilde{\tau}_L$, $M_{\tilde{F}'} = M_{\tilde{U}}$, $M_{\tilde{D}}$, $M_{\tilde{E}}$

for $\tilde{f}_R = \tilde{t}_R, \tilde{b}_R, \tilde{\tau}_R$, respectively, and m_f is the mass of the corresponding fermion. From renormalization group equations [12] one expects that due to the Yukawa interactions the soft SUSY breaking masses $M_{\tilde{Q}}, M_{\tilde{U}}, M_{\tilde{D}}, M_{\tilde{L}}$, and $M_{\tilde{E}}$ of the 3^{rd} generation sfermions are smaller than those of the 1^{st} and 2^{nd} generation. Evidently, \tilde{t}_L - \tilde{t}_R mixing can be important because of the large top quark mass. For sbottoms and staus L-R mixing can be important if $\tan\beta \gtrsim 10$. The mass eigenvalues for the sfermions $\tilde{f} = \tilde{t}, \tilde{b}, \tilde{\tau}$ are

$$m_{\tilde{f}_{1,2}}^2 = \frac{1}{2} \left(m_{\tilde{f}_L}^2 + m_{\tilde{f}_R}^2 \mp \sqrt{(m_{\tilde{f}_L}^2 - m_{\tilde{f}_R}^2)^2 + 4m_f^2 a_f^2} \right) \quad (5)$$

where \tilde{t}_1, \tilde{b}_1 and $\tilde{\tau}_1$ denote the lighter eigenstates. The mixing angles $\theta_{\tilde{f}}$ are given by

$$\cos\theta_{\tilde{f}} = \frac{-a_f m_f}{\sqrt{(m_{\tilde{f}_L}^2 - m_{\tilde{f}_1}^2)^2 + a_f^2 m_f^2}}, \quad \sin\theta_{\tilde{f}} = \frac{m_{\tilde{f}_L}^2 - m_{\tilde{f}_1}^2}{\sqrt{(m_{\tilde{f}_L}^2 - m_{\tilde{f}_1}^2)^2 + a_f^2 m_f^2}}. \quad (6)$$

Hence, in the convention used we have $|\cos\theta_{\tilde{f}}| > \frac{1}{\sqrt{2}}$ if $m_{\tilde{f}_L} < m_{\tilde{f}_R}$ and $|\cos\theta_{\tilde{f}}| < \frac{1}{\sqrt{2}}$ if $m_{\tilde{f}_R} < m_{\tilde{f}_L}$.

The mass of the τ -sneutrino is

$$m_{\tilde{\nu}_\tau}^2 = M_L^2 + \frac{1}{2} m_Z^2 \cos 2\beta. \quad (7)$$

The inversions of eqs. (2) to (7) are

$$M_{\tilde{Q}}^2 = m_{\tilde{t}_2}^2 \sin^2 \theta_{\tilde{t}} + m_{\tilde{t}_1}^2 \cos^2 \theta_{\tilde{t}} - m_Z^2 \cos 2\beta \left(\frac{1}{2} - \frac{2}{3} \sin^2 \theta_W \right) - m_t^2 \quad (8)$$

$$M_{\tilde{U}}^2 = m_{\tilde{t}_1}^2 \sin^2 \theta_{\tilde{t}} + m_{\tilde{t}_2}^2 \cos^2 \theta_{\tilde{t}} - \frac{2}{3} m_Z^2 \cos 2\beta \sin^2 \theta_W - m_t^2 \quad (9)$$

$$M_{\tilde{Q}}^2 = m_{\tilde{b}_2}^2 \sin^2 \theta_{\tilde{b}} + m_{\tilde{b}_1}^2 \cos^2 \theta_{\tilde{b}} + m_Z^2 \cos 2\beta \left(\frac{1}{2} - \frac{1}{3} \sin^2 \theta_W \right) - m_b^2 \quad (10)$$

$$M_{\tilde{D}}^2 = m_{\tilde{b}_1}^2 \sin^2 \theta_{\tilde{b}} + m_{\tilde{b}_2}^2 \cos^2 \theta_{\tilde{b}} + \frac{1}{3} m_Z^2 \cos 2\beta \sin^2 \theta_W - m_b^2 \quad (11)$$

$$M_{\tilde{L}}^2 = m_{\tilde{\tau}_2}^2 \sin^2 \theta_{\tilde{\tau}} + m_{\tilde{\tau}_1}^2 \cos^2 \theta_{\tilde{\tau}} + m_Z^2 \cos 2\beta \left(\frac{1}{2} - \sin^2 \theta_W \right) - m_\tau^2 \quad (12)$$

$$M_{\tilde{E}}^2 = m_{\tilde{\tau}_1}^2 \sin^2 \theta_{\tilde{\tau}} + m_{\tilde{\tau}_2}^2 \cos^2 \theta_{\tilde{\tau}} + m_Z^2 \cos 2\beta \sin^2 \theta_W - m_\tau^2 \quad (13)$$

$$M_{\tilde{L}}^2 = m_{\tilde{\nu}_\tau}^2 - \frac{1}{2} m_Z^2 \cos 2\beta \quad (14)$$

$$a_f m_f = (m_{\tilde{f}_1}^2 - m_{\tilde{f}_2}^2) \sin \theta_{\tilde{f}} \cos \theta_{\tilde{f}} \quad (15)$$

The soft-breaking parameter $M_{\tilde{Q}}$ enters the equations of $m_{\tilde{t}_L}$ and $m_{\tilde{b}_L}$. Therefore eqs. (8) and (10) imply the following condition (at tree-level):

$$m_W^2 \cos 2\beta = m_{\tilde{t}_2}^2 \sin^2 \theta_{\tilde{t}} + m_{\tilde{t}_1}^2 \cos^2 \theta_{\tilde{t}} - m_{\tilde{b}_2}^2 \sin^2 \theta_{\tilde{b}} - m_{\tilde{b}_1}^2 \cos^2 \theta_{\tilde{b}} - m_t^2 + m_b^2. \quad (16)$$

This condition shows that if $\tan\beta$ and five of the six measurable parameters $m_{\tilde{t}_1}, m_{\tilde{t}_2}, \cos^2 \theta_{\tilde{t}}, m_{\tilde{b}_1}, m_{\tilde{b}_2}$, and $\cos^2 \theta_{\tilde{b}}$ are known, the sixth can be predicted. An analogous condition holds for $M_{\tilde{L}}$ in the slepton sector due to eqs. (12) and (14). Furthermore, from eqs. (6) and (15) one can see that, in the convention used, a_f and $\cos\theta_{\tilde{f}}$ have opposite signs.

2.2 Cross Sections for $e^+e^- \rightarrow \tilde{f}_i \bar{\tilde{f}}_i$

The reaction $e^+e^- \rightarrow \tilde{f}_i \bar{\tilde{f}}_i$ proceeds via γ and Z exchange. The tree-level cross section at a center-of-mass energy \sqrt{s} is given by [18, 19, 13]:

$$\sigma^{tree} = \frac{\pi\alpha^2 N_C}{3s} \beta^3 \left[Q_f^2 + \left(\frac{(v_e^2 + a_e^2) v_{\tilde{f}_i}^2}{16 s_W^4 c_W^4} s^2 - \frac{Q_f v_e v_{\tilde{f}_i}}{2 s_W^2 c_W^2} s (s - m_Z^2) \right) \frac{1}{(s - m_Z^2)^2 + \Gamma_Z^2 m_Z^2} \right] \quad (17)$$

where $s_W^2 = 1 - c_W^2 = \sin^2 \theta_W$, $v_e = 2 \sin^2 \theta_W - \frac{1}{2}$, and $a_e = -\frac{1}{2}$. N_C is a colour factor which is 3 for squarks and 1 for sleptons. The tree-level cross section has the typical β^3 kinematic suppression where $\beta = (1 - 4m_{\tilde{f}_i}^2/s)^{1/2}$ is the velocity of the outgoing scalar particles. The Z coupling to $\tilde{f}_i \bar{\tilde{f}}_i$ is proportional $v_{\tilde{f}_i}$ with $v_{\tilde{f}_1} = 2(I_f^3 \cos^2 \theta_{\tilde{f}} - Q_f \sin^2 \theta_W)$, $v_{\tilde{f}_2} = 2(I_f^3 \sin^2 \theta_{\tilde{f}} - Q_f \sin^2 \theta_W)$, where I_f^3 and Q_f are the third component of the weak isospin and the charge of the fermion f ($Q_e = -1$). This coupling vanishes at the mixing angles $\cos^2 \theta_{\tilde{f}} = 0.31, 0.16$, and 0.46 for \tilde{t}_1 , \tilde{b}_1 , and $\tilde{\tau}_1$, respectively. Note that the sign of $\cos \theta_{\tilde{f}}$ cannot be determined from the cross section (17), as this depends only on $\cos^2 \theta_{\tilde{f}}$.

The interference between the γ and Z exchange contributions leads to a characteristic minimum of the cross sections for $e^+e^- \rightarrow \tilde{f}_i \bar{\tilde{f}}_i$ which occurs at a specific value of the mixing angles $\theta_{\tilde{f}}$ given by

$$\cos^2 \theta_{\tilde{f}}|_{min} = \frac{e_f}{T_f^3} \sin^2 \theta_W [1 + (1 - s/m_Z^2) F(\sin^2 \theta_W)] \quad (18)$$

where $F(\sin^2 \theta_W) = \cos^2 \theta_W (L_e + R_e)/(L_e^2 + R_e^2) \approx -0.22$, $F(\sin^2 \theta_W) = \cos^2 \theta_W/L_e \approx -2.9$, and $F(\sin^2 \theta_W) = \cos^2 \theta_W/R_e \approx 3.3$, for unpolarized, left- and right-polarized e^- beams, respectively, with $L_e = -\frac{1}{2} + \sin^2 \theta_W$ and $R_e = \sin^2 \theta_W$. For polarized e^- beams the dependence on the mixing angles is much more pronounced than for unpolarized beams. The corresponding minimum of the $e^+e^- \rightarrow \tilde{f}_2 \bar{\tilde{f}}_2$ cross sections occurs at $1 - \cos^2 \theta_{\tilde{f}}|_{min}$.

In the calculations of the cross sections we have also included SUSY-QCD corrections taking the formulae of [20] (see also [18, 21, 22]) with $\alpha_s(M_Z) = 0.12$, $m_t = 175$ GeV, and corrections due to initial state radiation [23].

Figure 1a shows contour lines of the total $e^+e^- \rightarrow \tilde{t}_1 \bar{\tilde{t}}_1$ cross section in the $m_{\tilde{t}_1} - \cos \theta_{\tilde{t}}$ plane for $\sqrt{s} = 500$ GeV and unpolarized beams. For the calculation of the SUSY-QCD radiative corrections we have assumed $m_{\tilde{t}_2} = m_{\tilde{g}} = 300$ GeV. Significantly above the threshold there is a clear dependence on $\cos \theta_{\tilde{t}}$. Figure 1b shows the $\cos \theta_{\tilde{t}}$ dependence of the $e^+e^- \rightarrow \tilde{t}_1 \bar{\tilde{t}}_1$ cross section for left- and right-polarized as well as for unpolarized e^- beams for $\sqrt{s} = 500$ GeV and $m_{\tilde{t}_1} = 180$ GeV. For

both left- and right-polarized e^- beams the cross sections depend strongly on the mixing angle. It is important to note that this dependence is opposite for left and right polarization. Therefore, experiments with polarized e^- beams will allow a more precise determination of the mass $m_{\tilde{t}_1}$ and the mixing angle $\theta_{\tilde{t}}$.

Figure 2 a shows contour lines of the total cross section of $e^+e^- \rightarrow \tilde{t}_2\tilde{t}_2$ in the $m_{\tilde{t}_2} - \cos^2\theta_{\tilde{t}}$ plane at $\sqrt{s} = 2$ TeV. The $\cos\theta_{\tilde{t}}$ dependence of this cross section at $\sqrt{s} = 2$ TeV for left- and right-polarized and unpolarized e^- beams is shown in Fig. 2 b for $m_{\tilde{t}_2} = 700$ GeV. Again, the $\cos\theta_{\tilde{t}}$ dependence is much stronger for polarized than for unpolarized beams, however, the behavior is opposite to that of $e^+e^- \rightarrow \tilde{t}_1\tilde{t}_1$. For the calculation of the SUSY-QCD radiative corrections we assumed $m_{\tilde{t}_1} = 300$ GeV and $m_{\tilde{g}} = 700$ GeV.

We shall discuss in Section 6 how experimental data on cross sections with left- and right-polarized beams would allow to determine masses and mixing angles, and then give information on soft SUSY breaking parameters.

Figure 3 a shows the contour plot of the total cross section of $e^+e^- \rightarrow \tilde{b}_1\tilde{b}_1$ in the $m_{\tilde{b}_1} - \cos\theta_{\tilde{b}}$ plane at $\sqrt{s} = 500$ GeV for unpolarized beams. For a polarized e^- beam the $\cos\theta_{\tilde{b}}$ dependence of the cross sections is much stronger, as shown in Fig. 3 b for $m_{\tilde{b}_1} = 180$ GeV and $\sqrt{s} = 500$ GeV.

Contour lines for the cross section of $e^+e^- \rightarrow \tilde{\tau}_1\tilde{\tau}_1$ in the $m_{\tilde{\tau}_1} - \cos\theta_{\tilde{\tau}}$ plane at $\sqrt{s} = 500$ GeV are shown in Fig. 4 a. Figure 4 b shows the cross section for polarized and unpolarized e^- beams as a function of $\cos\theta_{\tilde{\tau}}$ for $m_{\tilde{\tau}_1} = 180$ GeV and $\sqrt{s} = 500$ GeV. For both beam polarizations these cross sections again exhibit a strong dependence on the mixing angle.

Figure 5 shows the $m_{\tilde{\nu}}$ dependence of the cross section for $e^+e^- \rightarrow \tilde{\nu}_\tau\tilde{\nu}_\tau$ for unpolarized as well as left- and right-polarized e^- beams. Since the $\tilde{\nu}_\tau$ is not mixed, the polarization dependence is entirely due to the different Ze^+e^- couplings.

The \sqrt{s} dependence of the $e^+e^- \rightarrow \tilde{t}_1\tilde{t}_1$ cross section is shown in Fig. 6 for $m_{\tilde{t}_1} = 180$ GeV and $\cos\theta_{\tilde{t}} = 0.7$. The effect of SUSY-QCD corrections for $e^+e^- \rightarrow \tilde{t}_1\tilde{t}_1$ from gluon and gluino exchange as well as the initial state radiation correction as a function of \sqrt{s} is demonstrated in Fig. 7, for $\cos\theta_{\tilde{t}} = 0.7$, $m_{\tilde{t}_1} = 180$ GeV, and $m_{\tilde{t}_2} = m_{\tilde{g}} = 300$ GeV. Note that at high energies the gluino exchange contribution has the opposite sign of the gluon exchange contribution, and the absolute values are increasing with \sqrt{s} . The effects are similar for $e^+e^- \rightarrow \tilde{b}_1\tilde{b}_1$. A detailed discussion of SUSY-QCD corrections is given in [20]. The effect due to initial state radiation turns out to be of the order of 10 %. The sum of all corrections can well exceed 10%.

3 Decays of Stop, Sbottom, τ -Sneutrino, and Stau

The sfermions of the third generation can have the weak decays ($i, j = 1, 2; k = 1, \dots, 4$)

$$\tilde{t}_i \rightarrow t \tilde{\chi}_k^0, \quad b \tilde{\chi}_j^+ \quad (19)$$

$$\tilde{b}_i \rightarrow b \tilde{\chi}_k^0, \quad t \tilde{\chi}_j^- \quad (20)$$

$$\tilde{\tau}_i \rightarrow \tau \tilde{\chi}_k^0, \quad \nu_\tau \tilde{\chi}_j^+ \quad (21)$$

$$\tilde{\nu}_\tau \rightarrow \nu \tilde{\chi}_k^0, \quad \tau \tilde{\chi}_j^- \quad (22)$$

Owing to the Yukawa terms and the L–R mixing the decay patterns of stops, sbottoms, and staus will be different from those of the sfermions of the first two generations [24, 25]. Stops and sbottoms can also have the strong decays

$$\tilde{t}_i \rightarrow t \tilde{g}, \quad \tilde{b}_i \rightarrow b \tilde{g}. \quad (23)$$

They are dominant if they are kinematically allowed. Otherwise, the lighter squark mass eigenstates decay mostly according to (19) and (20). Moreover, in case of strong L–R mixing the splitting between the two mass eigenstates may be so large that the following additional decay modes are present [10]:

$$\tilde{t}_2 \rightarrow \tilde{t}_1 Z (h^0, H^0, A^0), \quad \tilde{b}_1 W^+ (H^+), \quad (24)$$

$$\tilde{b}_2 \rightarrow \tilde{b}_1 Z (h^0, H^0, A^0), \quad \tilde{t}_1 W^- (H^-), \quad (25)$$

$$\tilde{\tau}_2 \rightarrow \tilde{\tau}_1 Z, \quad \tilde{\nu}_\tau W^-. \quad (26)$$

If the \tilde{t}_1 is the lightest charged SUSY particle and $m_{\tilde{\chi}_1^0} + m_b + m_W < m_{\tilde{t}_1} < m_{\tilde{\chi}_1^0} + m_t$, the decay $\tilde{t}_1 \rightarrow b W^+ \tilde{\chi}_1^0$ can be dominant [26], otherwise the higher-order decay $\tilde{t}_1 \rightarrow c \tilde{\chi}_1^0$ dominates [19]. In the case that $m_{\tilde{\tau}_1} < m_{\tilde{t}_1}$ also $\tilde{t}_1 \rightarrow b \nu_\tau \tilde{\tau}_1$ and in case that $m_{\tilde{\nu}} < m_{\tilde{t}_1}$ also $\tilde{t}_1 \rightarrow b \tau^+ \tilde{\nu}_\tau$ might be important.

Figure 8 a and 8 b show the parameter domains in the $M - \mu$ plane for the decays of \tilde{t}_1 and \tilde{b}_1 , eqs. (19) and (20), taking $m_{\tilde{t}_1} = 180$ GeV, $\tan \beta = 2$, and $m_{\tilde{b}_1} = 180$ GeV, $\tan \beta = 30$. In region (a) only the decay $\tilde{t}_1 \rightarrow c \tilde{\chi}_1^0$ is allowed, whereas in region (b) $\tilde{t}_1 \rightarrow c \tilde{\chi}_1^0$ and $\tilde{t}_1 \rightarrow b W^+ \tilde{\chi}_1^0$ are possible. In the small stripe of region (c) also $\tilde{t}_1 \rightarrow c \tilde{\chi}_2^0$ is possible. In region (d) the decay $\tilde{t}_1 \rightarrow b \tilde{\chi}_1^+$ has practically 100% branching ratio. This is further illustrated in Fig. 9 a where we plot the branching ratios for \tilde{t}_1 decays as a function of M for $\mu = -500$ GeV, $m_{\tilde{t}_1} = 180$ GeV, $\tan \beta = 2$, and $\cos \theta_{\tilde{t}} = 0.7$. The parameter domains for the $\tilde{\tau}_1$ decays into neutralinos are almost identical to those of the corresponding \tilde{b}_1 decays, if the masses of $\tilde{\tau}_1$ and \tilde{b}_1 are equal.

Figure 9 b shows the branching ratios for \tilde{b}_1 decays as a function of M for $m_{\tilde{b}_1} = 180$ GeV, $\tan \beta = 30$, $\cos \theta_{\tilde{t}} = 0.7$, and $\mu = -500$ GeV. Figure 10 a and 10 b show the branching ratios for \tilde{b}_1 and $\tilde{\tau}_1$ decays as a function of M for $\mu = -130$ GeV and $m_{\tilde{b}_1} = m_{\tilde{\tau}_1} = 180$ GeV, $\tan \beta = 30$, $\cos \theta_{\tilde{b}} = \cos \theta_{\tilde{\tau}} = 0.7$. Similarly, Figure 10 c

shows the branching ratios for $\tilde{\nu}_\tau$ decays taking $m_{\tilde{\nu}_\tau} = 180$ GeV, $\tan\beta = 2$, and $\mu = -130$ GeV. The LSP decays of \tilde{b}_1 and $\tilde{\tau}_1$ are about 60% and 40%, respectively. The branching ratio for the visible decays of the $\tilde{\nu}_\tau$ is between 40% and 90%.

The decay patterns of the heavier sfermion mass-eigenstates can be quite complicated, because all the decay modes of eqs. (19) to (26) can occur. We calculate the different decay widths with the formulae of Refs. [10, 13, 26]. Figure 11 a and 11 b show the branching ratios for \tilde{t}_2 decays as a function of M for $m_{\tilde{t}_2} = 700$ GeV, taking $\tan\beta = 2$, $\mu = -1000$ GeV, $m_A = 150$ GeV, $M_{\tilde{Q}} = 607$ GeV, $M_{\tilde{U}} = 360$ GeV, $M_{\tilde{D}} = 850$ GeV, and $A_t = 500$ GeV. The masses and mixing parameters of the other particles involved then are $m_{\tilde{t}_1} = 258$ GeV, $\cos\theta_{\tilde{t}} = -0.468$, $m_{\tilde{b}_1} = 608$ GeV, $m_{\tilde{b}_2} = 851$ GeV, $\cos\theta_{\tilde{b}} = -0.999$, $m_{h^0} = 98$ GeV, $m_{H^0} = 165$ GeV, $m_{H^\pm} = 169$ GeV, $\cos\alpha = 0.535$. We have included radiative corrections to the Higgs masses and the Higgs mixing angle according to [27]. For $M \lesssim 200$ GeV the decay $\tilde{t}_2 \rightarrow t\tilde{g}$ dominates, whereas for $M \gtrsim 200$ GeV the decay $\tilde{t}_2 \rightarrow Z\tilde{t}_1$ has the largest branching fraction. It is interesting to note that in this case the decays $\tilde{t}_2 \rightarrow A^0\tilde{t}_1$ and $\tilde{t}_2 \rightarrow H^0\tilde{t}_1$ have larger branching ratios than the decay into $b\tilde{\chi}_1^+$ which is the most important decay mode of \tilde{t}_1 .

Figure 12 a and 12 b show the branching ratios of the \tilde{b}_2 decays for $m_{\tilde{b}_2} = 700$ GeV, $\tan\beta = 30$, $\mu = -1000$ GeV, $m_A = 150$ GeV, $M_{\tilde{Q}} = 637$ GeV, $M_{\tilde{U}} = 320$ GeV, $M_{\tilde{D}} = 450$ GeV, and $A_t = 500$ GeV. The masses and mixing parameters of the other particles involved then are $m_{\tilde{b}_1} = 350$ GeV, $\cos\theta_{\tilde{b}} = -0.469$, $m_{\tilde{t}_1} = 324$ GeV, $m_{\tilde{t}_2} = 678$ GeV, $\cos\theta_{\tilde{t}} = -0.273$, $m_{h^0} = 118$ GeV, $m_{H^0} = 146$ GeV, $m_{H^\pm} = 176$ GeV, and $\cos\alpha = 0.998$. In this example the transition $\tilde{b}_2 \rightarrow H^-\tilde{t}_1$ is dominant for $M \gtrsim 200$ GeV, and $\tilde{b}_2 \rightarrow Z\tilde{b}_1$ and $\tilde{b}_2 \rightarrow W^-\tilde{t}_1$ have larger branching ratios than $\tilde{b}_2 \rightarrow t\tilde{\chi}_1^+$ or $\tilde{b}_2 \rightarrow b\tilde{\chi}_{1,2}^0$. The branching ratios for the decays of the sleptons $\tilde{\tau}_2$ and $\tilde{\nu}_\tau$ are shown in Figs. 13 a, b, and Figs. 14 a, b, for $m_{\tilde{\tau}_2} = 700$ GeV and $m_{\tilde{\nu}_\tau} = 687$ GeV, respectively, taking $\tan\beta = 30$, $\mu = -1000$ GeV, $m_A = 150$ GeV, $M_{\tilde{L}} = 690$ GeV, $M_{\tilde{E}} = 490$ GeV, and $A_\tau = 500$ GeV. The mass of the lighter stau then is $m_{\tilde{\tau}_1} = 480$ GeV, and the mixing angle is $\cos\theta_{\tilde{\tau}} = -0.213$. The Higgs boson masses are the same as in Fig. 12. In these examples, the $\tilde{\tau}_2$ and $\tilde{\nu}_\tau$ decays into charginos and neutralinos have large branching ratios, and the decays $\tilde{\tau}_2 \rightarrow \nu\tilde{\chi}_1^-$ and $\tilde{\nu}_\tau \rightarrow \tau\tilde{\chi}_1^+$ dominate. The decay $\tilde{\tau}_2 \rightarrow Z\tilde{\tau}_1$ has a branching ratio of 5% to 10%, and $\tilde{\nu}_\tau \rightarrow \tau\tilde{\chi}_1^+$ has a branching ratio of 35% to 55%. It is interesting to note that in this example the branching ratio of the invisible decays mode $\tilde{\nu}_\tau \rightarrow \nu_\tau\tilde{\chi}_1^0$ is always less than about 18%.

Quite generally, the decay widths of the \tilde{t}_i , \tilde{b}_i , and $\tilde{\tau}_i$ decays into neutralinos and charginos, eq. (19) to (21), depend also on the sign of $\cos\theta_{\tilde{f}}$. It may therefore be possible to determine the sign of the mixing angle by studying these decays.

Table 1 lists the most important signatures for \tilde{t}_1 , \tilde{b}_1 , $\tilde{\nu}_\tau$, and $\tilde{\tau}_1$ for $\sqrt{s} = 500$ GeV. If the decays $\tilde{t}_1 \rightarrow b\tilde{\chi}_1^+$ or $\tilde{\tau}_1 \rightarrow \nu_\tau\tilde{\chi}_1^-$ occur, the $\tilde{\chi}_1^\pm$ will most probably be discovered first and thus its mass and couplings will be known. The decay $\tilde{t}_1 \rightarrow bW^+\tilde{\chi}_1^0$ leads to the same final states as $\tilde{t}_1 \rightarrow b\tilde{\chi}_1^+$ (provided $\tilde{\chi}_1^+ \rightarrow H^+\tilde{\chi}_1^0$ is not allowed). The decay $\tilde{\nu}_\tau \rightarrow \nu\tilde{\chi}_1^0$ is invisible. Thus, one-sided events can occur where one $\tilde{\nu}_\tau$ decays invisibly

and the other one decays visibly into one of the final states given in table 1.

Channel	Signatures
$\tilde{t}_1 \rightarrow b \tilde{\chi}_1^+$	1 b -jet + 1 ℓ^+ + \cancel{p}_T , 1 b -jet + 2 jets + \cancel{p}_T
$\tilde{t}_1 \rightarrow c \tilde{\chi}_1^0$	1 jet + \cancel{p}_T
$\tilde{b}_1 \rightarrow b \tilde{\chi}_1^0$	1 b -jet + \cancel{p}_T
$\tilde{b}_1 \rightarrow b \tilde{\chi}_2^0$	1 b -jet + $\ell^+ \ell^-$ + \cancel{p}_T , 1 b -jet + 2 jets + \cancel{p}_T
$\tilde{\tau}_1 \rightarrow \tau \tilde{\chi}_1^0$	τ + \cancel{p}_T
$\tilde{\tau}_1 \rightarrow \tau \tilde{\chi}_2^0$	τ + $\ell^+ \ell^-$ + \cancel{p}_T , τ + 2 jets + \cancel{p}_T
$\tilde{\tau}_1^- \rightarrow \nu_\tau \tilde{\chi}_1^-$	ℓ^- + \cancel{p}_T , 2 jets + \cancel{p}_T
$\tilde{\nu}_\tau \rightarrow \tau^- \tilde{\chi}_1^+$	τ^- + ℓ^+ + \cancel{p}_T , τ^- + 2 jets + \cancel{p}_T
$\tilde{\nu}_\tau \rightarrow \nu \tilde{\chi}_2^0$	$\ell^+ \ell^-$ + \cancel{p}_T , 2 jets + \cancel{p}_T , γ + \cancel{p}_T

Table 1: Expected signatures for \tilde{t}_1 , \tilde{b}_1 , $\tilde{\nu}_\tau$, and $\tilde{\tau}_1$ production for $\sqrt{s} = 500$ GeV. Owing to pair production all combinations of the corresponding signatures may occur.

4 Stop Event Generation

In this section we describe the event generator for $e^+e^- \rightarrow \tilde{t}_1 \tilde{t}_1^*$ with the stop decay modes $\tilde{t}_1 \rightarrow c \tilde{\chi}_1^0$ and $\tilde{t}_1 \rightarrow b \tilde{\chi}_1^+$. The chargino decays via $\tilde{\chi}_1^+ \rightarrow W^+ \tilde{\chi}_1^0$, where W^+ can be either virtual or real. The event generator is based on the calculation of the 4-momenta distributions of the stop decay products $\tilde{\chi}_1^0 c$ $\tilde{\chi}_1^0 \bar{c}$ and $\tilde{\chi}_1^+ b$ $\tilde{\chi}_1^- \bar{b}$. The large effects of QCD corrections are included in the cross section calculation. Stop production and decay have been defined as new processes in the PYTHIA program package [28]. The event generation process includes the modelling of hadronic final states.

In the first step of the event generation, initial state photons are emitted using the program package REMT [28] which takes into account the expected stop cross section from zero to the nominal center-of-mass energy. Beamstrahlung photons are generated using the beam parameters of the NLC 1992 design. The effective center-of-mass energy is calculated for the initial production of the 4-momenta of the final-state particles. These 4-momenta are then boosted to the lab-frame according to the momentum of the emitted photons. For the hadronization process of the $c\bar{c}$ in the $\tilde{\chi}_1^0 c$ $\tilde{\chi}_1^0 \bar{c}$ and of the $b\bar{b}$ in the $\tilde{\chi}_1^+ b$ $\tilde{\chi}_1^- \bar{b}$ decay mode, a color string with invariant mass of the quark-antiquark-system is defined. The possible gluon emission and hadronization are performed using the Lund model of string fragmentation with the PYTHIA program package [28]. The Peterson *et al.* [29] fragmentation parameters for the c - and b -quarks are used: $\epsilon_c = 0.03$ and $\epsilon_b = 0.0035$. Finally, short-lived particles decay into their observable final state. Details of the event generator are given in [30].

5 Simulation and Selection

The investigated background reactions and their cross sections are shown in Fig. 15. They are simulated for $\mathcal{L} = 10 \text{ fb}^{-1}$, and 1000 signal events are simulated in the $\tilde{\chi}_1^0 c \tilde{\chi}_1^0 \bar{c}$ and $\tilde{\chi}_1^+ b \tilde{\chi}_1^- \bar{b}$ decay channels. The L3 detector at CERN including the upgrades for LEP2 served as an example for an e^+e^- 500 GeV detector. Details of the parametric detector simulation are given in [31]. An important feature is the overall hadronic energy resolution of about 7%.

In both channels, the $\tilde{\chi}_1^0$'s escape the detector and cause large missing energy. In the case of $\tilde{\chi}_1^0 c \tilde{\chi}_1^0 \bar{c}$, the c -quarks form mostly two acoplanar jets. A mass combination of $M_{t_1} = 180 \text{ GeV}$ and $m_{\tilde{\chi}_1^0} = 100 \text{ GeV}$ is investigated in detail. For $\tilde{\chi}_1^+ b \tilde{\chi}_1^- \bar{b}$ on average the visible energy is larger. In this channel, the mass combination $M_{t_1} = 180 \text{ GeV}$, $m_{\tilde{\chi}_1^+} = 150 \text{ GeV}$, and $m_{\tilde{\chi}_1^0} = 60 \text{ GeV}$ has been studied. Typically four jets are formed, two from the b -quarks, and two from the boosted W 's.

In the first step of the event selection, unbalanced hadronic events are selected using the following selection requirements:

$$25 < \text{hadronic clusters} < 110, \quad 0.2 < E_{\text{vis}}/\sqrt{s} < 0.7, \\ E_{\parallel}^{\text{imb}}/E_{\text{vis}} < 0.5, \quad \text{Thrust} < 0.95, \quad |\cos \theta_{\text{Thrust}}| < 0.7 .$$

Channel	$\tilde{\chi}_1^0 c \tilde{\chi}_1^0 \bar{c}$	$\tilde{\chi}_1^+ b \tilde{\chi}_1^- \bar{b}$	qq	WW	eW ν	tt	ZZ	eeZ
Total (in 1000)	1	1	125	70	50	7	6	60
After preselection (in 1000)	0.4	0.7	1.7	2.2	3.2	1.3	0.2	0.3

Table 2: Expected events per 10 fb^{-1} at $\sqrt{s} = 500 \text{ GeV}$, and number of events after the preselection as defined in the text.

A large part of the background of back-to-back events without missing energy is rejected. Table 2 shows the number of initially produced events per $\mathcal{L} = 10 \text{ fb}^{-1}$ at $\sqrt{s} = 500 \text{ GeV}$, and the number of events which pass this preselection. The requirement of a large number of hadronic clusters removes e^+e^- , $\mu^+\mu^-$, and most of the $\tau^+\tau^-$ events. The minimum energy cut reduces most of the $\gamma\gamma$ events and ensures almost 100% trigger efficiency. The background from $\gamma\gamma$ events can, in addition, be strongly reduced by rejecting events where a scattered initial electron is detected at low angles. The upper energy cut reduces all standard background reactions. Beam gas events and events where much energy goes undetected along the beam axis are removed by rejection of events with very large parallel imbalance. The thrust cut removes remaining $\tau^+\tau^-$ events and reduces largely $q\bar{q}$ and $Z^0 Z^0$ background. The $\cos \theta_{\text{Thrust}}$ cut removes events where most probably much energy escapes undetected along the beam axis.

The final $\tilde{\chi}_1^0 c \tilde{\chi}_1^0 \bar{c}$ event selection is summarized in Table 3. The following cuts are applied:

- A hard upper energy cut reduces all standard background except $eW\nu$ (Fig. 16).
- Jets are clustered using the JADE algorithm. The y-cut value is optimized to obtain two jets for the signal.
- Semileptonic decays of the top quark can induce missing energy. These events are partly removed by requiring no isolated electron or muon.
- Events with large longitudinal energy imbalance are removed where probably much energy escapes undetected along the beam axis.
- The invariant mass of the two jets is required to be larger than 120 GeV to remove almost entirely $eW\nu$ events (Fig. 17).
- The acoplanarity angle is defined as the angle between the jets in the plane perpendicular to the beam axis. A maximum value of 2.9 rad is important to reduce the remaining background.

The result of this study is 4.3% detection efficiency and 9 background events. A detection confidence level of 3σ (99.73%) is expected for a cross section of 23 fb. Expected signal and background are shown in Fig. 18.

Channel	$\tilde{\chi}_1^0 c \tilde{\chi}_1^0 \bar{c}$	qq	WW	eW ν	tt	ZZ	eeZ
Total (in 1000)	1	125	70	50	7	6	60
After Preselection	391	1652	2163	3185	1259	182	318
$E_{vis}/\sqrt{s} < 0.4$	332	202	285	3032	70	4	98
Njet = 2	293	172	182	2892	17	3	72
No isolated e or μ	218	152	98	2757	5	3	9
$E_{\parallel}^{imb}/E_{vis} < 0.3$	185	101	70	2049	5	2	4
Invariant mass of jets > 120 GeV	52	25	12	7	1	0	0
Acoplanarity < 2.9 rad	43	0	5	3	1	0	0

Table 3: Final event selection cuts, expected signal efficiencies, and the number of expected background events. Bold face numbers indicate major background reductions.

The final $\tilde{\chi}_1^+ b \tilde{\chi}_1^- \bar{b}$ event selection is summarized in Table 4. Here the cuts are:

- A hard lower energy cut reduces most of the $eW\nu$ background.
- Topologies with back-to-back jets are reduced by an upper cut on the event thrust (Fig. 19).
- A lower cut on the number of hadronic clusters reduces efficiently low-multiplicity background final states (Fig. 20).
- Jets are clustered using the JADE algorithm. The y-cut value is optimized to obtain four jets for the signal.
- Events with an isolated electron or muon are rejected.
- An upper cut on the visible energy reduces $q\bar{q}$, W^+W^- , and $t\bar{t}$ background.
- Finally, the remaining $t\bar{t}$ background events are reduced by requiring less than 30% perpendicular energy imbalance.

Concerning the number of b -quarks per event, the decay $\tilde{\chi}_1^+ b \tilde{\chi}_1^- \bar{b} \rightarrow W^+ \tilde{\chi}_1^0 b W^- \tilde{\chi}_1^0 \bar{b}$ leads to the same final states as expected for $t\bar{t}$ background. Therefore, the tagging of b -quarks has not proved to be efficient to reduce this background.

The result of this study is 4.5% detection efficiency and 8 background events. A detection confidence level of 3σ (99.73%) is expected for a cross section of 19 fb. Expected signal and background are shown in Fig. 21.

Channel	$\tilde{\chi}_1^+ b \tilde{\chi}_1^- \bar{b}$	qq	WW	eW ν	tt	ZZ	eeZ
Total (in 1000)	1	125	70	50	7	6	60
After Preselection	695	1652	2163	3185	1259	182	318
$E_{vis}/\sqrt{s} > 0.35$	610	1494	2011	337	1234	178	239
Thrust < 0.85	536	326	420	24	1141	69	137
Ncluster ≥ 60	399	195	134	0	769	41	3
Njet = 4	211	53	72	0	432	22	0
No isolated e or μ	99	41	49	0	105	16	0
$E_{vis}/\sqrt{s} < 0.55$	57	3	8	0	23	0	0
$E_{\perp}^{imb}/E_{vis} < 0.3$	45	1	3	0	4	0	0

Table 4: Final event selection cuts, expected signal efficiencies, and the number of expected background events. Bold face numbers indicate major background reductions.

At a future e^+e^- collider with $\sqrt{s} = 500$ GeV, a large discovery potential for scalar top quarks is already expected within one year of data-taking ($\mathcal{L} = 10 \text{ fb}^{-1}$). Detector performances known from LEP detectors result in good background reduction. Full hermeticity of the detector is essential.

The confidence levels for discovering a signal are shown in Figs. 22 a and 22 b for the $\tilde{\chi}_1^+ b \tilde{\chi}_1^- \bar{b}$ and $\tilde{\chi}_1^0 c \tilde{\chi}_1^0 \bar{c}$ channels, respectively. Here, the confidence levels are given in $\sigma = N_{\text{expected}}/\sqrt{N_{\text{background}}}$. The sensitivity is sufficient to discover a 200 GeV stop independently of the values of the mixing angle with 3σ in both $\tilde{\chi}_1^0 c$ and $\tilde{\chi}_1^+ b$ decay modes for the investigated neutralino and chargino mass combinations. A complete set of mass combinations remains to be studied.

At a later stage, the total luminosity could reach 50 fb^{-1} , and the resulting discovery region for a 3σ effect is shown in Fig. 23. An increase of the center-of-mass energy would extend the discovery region further as shown in Fig. 24 for $\sqrt{s} = 800$ GeV $\mathcal{L} = 200 \text{ fb}^{-1}$. Based on experience made in the LEP2 searches [32] the efficiency for the simulated mass combination can be extended to a larger mass region for $m_{\tilde{t}_1} - m_{\tilde{\chi}_1^\pm} > 20 \text{ GeV}$.

6 Determination of Soft–Breaking Parameters — A Case Study

In this section we want to estimate the experimental accuracies for the stop and sbottom masses and mixing angles which can be expected from the Monte Carlo simulation described in the preceding sections. Without beam polarization a possible way to determine $m_{\tilde{t}_1}$ and $\cos\theta_{\tilde{t}}$ is using the \sqrt{s} and $\cos\theta_{\tilde{t}}$ dependence of the unpolarized $e^+e^- \rightarrow \tilde{t}_1\tilde{t}_1^*$ total cross section (see Figs. 1a and 6). Let us take as reference point $m_{\tilde{t}_1} = 180$ GeV, $\cos\theta_{\tilde{t}} = 0.57$, and $\sqrt{s} = 400$ GeV and $\sqrt{s} = 500$ GeV as the two reference energies. Note that at $|\cos\theta_{\tilde{t}}| = 0.57$ the $e^+e^- \rightarrow \tilde{t}_1\tilde{t}_1^*$ cross section has its minimum. The cross sections at this point for these two energy values are $\sigma = 18.2 \pm 4.1$ fb at $\sqrt{s} = 400$ GeV and $\sigma = 47.4 \pm 5.5$ fb at $\sqrt{s} = 500$ GeV where the experimental errors follow from the Monte Carlo simulation. Figure 25 shows the corresponding error bands in the $m_{\tilde{t}_1} - \cos\theta_{\tilde{t}}$ plane. As can be seen, hardly an information can be obtained on the mixing angle.

The polarization of the e^- beam offers the possibility of measuring the sfermion masses and especially the mixing angles with much higher accuracy. The cross sections of $e^+e^- \rightarrow \tilde{t}_1\tilde{t}_1^*$ for 90% left- and right-polarized e^- beam at the reference point $m_{\tilde{t}_1} = 180$ GeV, $|\cos\theta_{\tilde{t}}| = 0.57$ for $\sqrt{s} = 500$ GeV are $\sigma_L = 48.6 \pm 6.0$ fb, $\sigma_R = 46.1 \pm 4.9$ fb, where the experimental errors are given by $\Delta\sigma/\sigma = N_{\text{signal}} / \sqrt{N_{\text{signal}} + N_{\text{background}}}$ with the number of signal and background events determined as described in the previous section. Figure 26 shows the corresponding error bands and the error ellipse in the $m_{\tilde{t}_1} - \cos\theta_{\tilde{t}}$ plane. The experimental accuracies obtained in this way for the mass of the lighter stop and the stop mixing angle are

$$m_{\tilde{t}_1} = 180 \pm 7 \text{ GeV}, \quad (27)$$

$$\cos\theta_{\tilde{t}} = 0.57 \pm 0.06. \quad (28)$$

We treat the sbottom system in an analogous way. Assuming that $\tan\beta$ is not too large we can neglect left–right mixing in the sbottom sector. In the “Minimal Supergravity–inspired Model” [33] one expects $m_{\tilde{b}_L} \lesssim m_{\tilde{b}_R}$, thus $\tilde{b}_1 = \tilde{b}_L$ and $\tilde{b}_2 = \tilde{b}_R$, i.e. $\cos\theta_{\tilde{b}} = 1$. As reference point of the sbottom system we take $m_{\tilde{b}_1} = 200$ GeV, $m_{\tilde{b}_2} = 220$ GeV. The cross sections for $e^+e^- \rightarrow \tilde{b}_1\tilde{b}_1^*$ with 90% left-polarized e^- beams and for $e^+e^- \rightarrow \tilde{b}_2\tilde{b}_2^*$ with 90% right-polarized e^- beams then are $\sigma_L(e^+e^- \rightarrow \tilde{b}_1\tilde{b}_1^*) = 61.1 \pm 6.4$ fb, $\sigma_R(e^+e^- \rightarrow \tilde{b}_2\tilde{b}_2^*) = 6.0 \pm 2.6$ fb, where the errors are again determined by our Monte Carlo procedure. The errors for the sbottom masses follow as:

$$m_{\tilde{b}_1} = 200 \pm 4 \text{ GeV}, \quad (29)$$

$$m_{\tilde{b}_2} = 220 \pm 10 \text{ GeV}. \quad (30)$$

With these values for $m_{\tilde{t}_1}$, $\cos\theta_{\tilde{t}}$, $m_{\tilde{b}_1}$, and $m_{\tilde{b}_2}$ we can use (16) and obtain the mass of the heavier stop \tilde{t}_2 if $\tan\beta$ is known from other experiments. Taking, for instance,

$\tan \beta = 2$ leads to

$$m_{\tilde{t}_2} = 289 \pm 15 \text{ GeV}. \quad (31)$$

Confirming this value by producing $\tilde{t}_2 \bar{\tilde{t}}_2$ at higher energies would be an independent test of the MSSM.

Assuming that also μ is known from an other experiment we are now able to calculate the underlying soft SUSY breaking parameters $M_{\tilde{Q}}, M_{\tilde{U}}, M_{\tilde{D}}, A_t$ and A_b for the squarks of the third family according to eqs. (8) to (15). Taking $\mu = -200 \text{ GeV}$, $\tan \beta = 2$, and $m_t = 175 \text{ GeV}$ we obtain the following values:

$$M_{\tilde{Q}} = 195 \pm 4 \text{ GeV}, \quad (32)$$

$$M_{\tilde{U}} = 138 \pm 26 \text{ GeV}, \quad (33)$$

$$M_{\tilde{D}} = 219 \pm 10 \text{ GeV}, \quad (34)$$

$$A_t = -236 \pm 38 \text{ GeV} \quad \text{if } \cos \theta_{\tilde{t}} > 0, \quad (35)$$

$$A_t = 36 \pm 38 \text{ GeV} \quad \text{if } \cos \theta_{\tilde{t}} < 0. \quad (36)$$

These results have to be compared with those of [5] and the second paper of [6], where the stop mass was determined by a kinematical reconstruction of the $b\tilde{\chi}_1^+$ decay.

7 Summary

In this article we have discussed the production of stop, sbottom, τ -sneutrino and stau pairs in e^+e^- annihilation in the energy range $\sqrt{s} = 500 \text{ GeV}$ to 2 TeV . We have presented numerical predictions within the Minimal Supersymmetric Standard Model for the production cross sections and the decay rates and analyzed their SUSY parameter dependence. If $\tan \beta \gtrsim 10$, not only the top Yukawa terms, but also the bottom and tau Yukawa terms have important effects. The production cross sections as well as the decay rates of stops, sbottoms and staus depend in a characteristic way on the mixing angles.

A Monte Carlo study of $e^+e^- \rightarrow \tilde{t}_1 \bar{\tilde{t}}_1$ at $\sqrt{s} = 500 \text{ GeV}$ with the decays $\tilde{t}_1 \rightarrow c\tilde{\chi}_1^0$ and $\tilde{t}_1 \rightarrow b\tilde{\chi}_1^+$ has been performed for $m_{\tilde{t}_1} = 180 \text{ GeV}$, $m_{\tilde{\chi}_1^0} = 100 \text{ GeV}$, and $m_{\tilde{t}_1} = 180 \text{ GeV}$, $m_{\tilde{\chi}_1^\pm} = 150 \text{ GeV}$, $m_{\tilde{\chi}_1^0} = 60 \text{ GeV}$, respectively. A suitable set of kinematical cuts has been applied to reduce the known background reactions. In addition, detection regions have been given.

We have also estimated the experimental accuracies for the masses of stops and sbottoms and the stop mixing angle from measurements of the polarized cross sections. Furthermore, we have made an estimate of the accuracies which can be obtained for the soft-breaking SUSY parameters.

In summary, an e^+e^- collider — especially with a polarized e^- beam — is an ideal machine for detecting and studying the scalar partners of the third generation quarks and leptons.

Acknowledgements

We thank our colleagues participating at the Workshop “ e^+e^- Collisions at TeV Energies: The Physics Potential” for many useful discussions. This work was supported by the “Fonds zur Förderung der wissenschaftlichen Forschung” of Austria, project no. P10843-PHY.

References

- [1] H.E. Haber, G.L. Kane, Phys. Rep. 117 (1985) 75
- [2] H. P. Nilles, Phys. Rep. 110 (1984) 1;
R. Barbieri, Riv. Nuov. Cim. 11 (1988) 1;
R. Arnowitt, P. Nath, in *Particles and Fields*, Proc. of the VII J. A. Swieca Summer School, Sao Paolo, Brazil, 1993, ed. O. Eboli, V. Rivelles (World Scientific, Singapore, 1993);
V. Barger, R. J. N. Phillips, in *Recent Advances in the Superworld*, Proc. of the International Workshop, Woodlands, Texas, 1993, ed. J. Lopez, D. Nanopoulos (World Scientific, Singapore, 1994);
Properties of SUSY Particles, ed. L. Cifarelli, V. Khoze (World Scientific, Singapore, 1993);
X. Tata, Lectures presented at TASI95, Univ. of Colorado, Boulder, 1995, hep-ph/9510287
- [3] A. Bartl, W. Majerotto, B. Mösslacher, Proc. of the Workshop “ e^+e^- Collisions at 500 GeV: The Physics Potential”, DESY 92-123B, p. 641, ed. P. M. Zerwas;
J. F. Grivaz, ibidem, p. 663;
C. VanderVelde, ibidem, p. 681;
R. Becker, R. Starosta, ibidem, p. 691;
R. Becker, C. VanderVelde, ibidem, DESY93-123C, p. 457
- [4] A. Bartl, H. Eberl, S. Kraml, W. Majerotto, W. Porod, A. Sopczak, Proc. of the Workshop “ e^+e^- Collisions at TeV Energies: The Physics Potential”, DESY 96-123D, p. 385, ed. P. M. Zerwas
- [5] H. Baer, R. Munroe, X. Tata, Phys. Rev. D54 (1996) 6735
- [6] T. Tsukamoto, K. Fujii, H. Murayama, M. Yamaguchi, Y. Okada, Phys. Rev. D 51 (1995) 3153;
M. N. Danielson et al., Proc. of the 1996 Snowmass Workshop on “New Directions for High Energy Physics”
- [7] J. Ellis, S. Rudaz, Phys. Lett. B128 (1983) 248

- [8] G. Altarelli, R. Rückl, Phys. Lett. B144 (1984) 126;
I. Bigi, S. Rudaz, Phys. Lett. B153 (1985) 335
- [9] M. Drees, M. M. Nojiri, Nucl. Phys. B 369 (1992) 54
- [10] A. Bartl, W. Majerotto, W. Porod, Z. Phys. C64 (1994) 499,
erratum Z. Phys. C68 (1995) 518
- [11] W. de Boer et al., Proc. of the Workshop “ e^+e^- Collisions at TeV Energies: The Physics Potential”, DESY 96-123D, p. 377, ed. P. M. Zerwas
- [12] for a review see, e. g., M. Drees, S. P. Martin, Wisconsin preprint MADPH-95-879, hep-ph/9504324
- [13] A. Bartl, H. Eberl, S. Kraml, W. Majerotto, W. Porod, preprint UWThPh-1996-18, HEPHY-PUB 642/96, hep-ph/9603410, to be publ. in Z. Phys. C
- [14] J. F. Gunion, H. E. Haber, Nucl. Phys. B272 (1986) 1
- [15] OPAL Collaboration, R. Akers et al., Phys. Lett. B337 (1994) 207
ALEPH Collaboration, Contribution #0416 to the International Europhysics Conference on High Energy Physics, Brussels, 1995;
J.-F. Grivaz, Rapporteur Talk, International Europhysics Conference on High Energy Physics, Brussels, 1995
- [16] L. Rolandi (ALEPH), H. Dijkstra (DELPHI), D. Strickland (L3), G. Wilson (OPAL), Joint Seminar on the First Results of LEP1.5, CERN, Dec. 12, 1995;
ALEPH Coll., Phys.Lett. B373 (1996) 246;
L3 Coll., H. Nowak and A. Sopczak, L3 Note 1962 (June 1996);
L3 Coll., B. Adeva et al., Phys. Lett. B377 (1996) 289;
OPAL Coll., S. Asai and S. Komamiya, OPAL Physics Note PN-205 (Feb. 1996);
OPAL Coll., K. Ackerstaff et al., CERN-PPE/96-133.
- [17] DØ Collaboration, F. Abachi et al., Phys. Rev. Lett. 76 (1996) 2222
- [18] M. Drees, K. I. Hikasa, Phys. Lett. B252 (1990) 127
- [19] K. I. Hikasa, M. Kobayashi, Phys. Rev. D36 (1987) 724
- [20] H. Eberl, A. Bartl, W. Majerotto, Nucl. Phys. B472 (1996) 481
- [21] W. Beenakker, R. Höpker, P. M. Zerwas, Phys. Lett. B349 (1995) 463
- [22] A. Arhrib, M. Capdequi-Peyranere, A. Djouadi, Phys. Rev. D 52 (1995) 1404
- [23] See e.g. M. Peskin, 17th SLAC Summer Institute, SLAC-PUB-5210 (1990)

- [24] H. Baer, V. Barger, D. Karatas, X. Tata, Phys. Rev. D 36 (1987) 96;
R. M. Barnett, J. F. Gunion, H. E. Haber, Phys. Rev. Lett. 60 (1988) 401; Phys.
Rev. D 37 (1988) 1892
- [25] A. Bartl, W. Majerotto, B. Mösslacher, N. Oshimo, S. Stippel, Phys. Rev. D43
(1991) 2214
- [26] W. Porod, T. Wöhrmann, hep-ph/9608472, to be publ. in Phys. Rev. D
- [27] J. Ellis, G. Ridolfi, F. Zwirner, Phys. Lett. B262 (1991) 477;
V. Barger, M. S. Berger, A. L. Stange, R. J. N. Phillips, Phys. Rev. D45 (1992)
4128
- [28] T. Sjöstrand, Comp. Phys. Comm. 82 (1994) 74
- [29] C. Peterson *et al.*, Phys. Rev. D27 (1983) 105
- [30] A. Sopczak in the Proc. of the workshop “Physics at LEP2”, Vol. 2, CERN 96-01,
eds.: G. Altarelli, T. Sjöstrand, F. Zwirner
- [31] A. Sopczak, Proc. of the workshop on “Physics and Experiments with Linear
 e^+e^- Colliders”, Waikoloa, Hawaii, eds. F. A. Harris, S. L. Olsen, S. Pakvasa, X.
Tata, (World Scientific, 1993) p. 666; Z. Phys. C65 (1995) 449
- [32] H. Nowak, A. Sopczak, L3 note #1962 (1996)
- [33] J. Amundson et al., Report of the Supersymmetry Theory Subgroup, 1996 Snow-
mass Workshop on “New Directions for High Energy Physics”

Figure Captions

Fig. 1a: Contour lines for the total cross section of $e^+e^- \rightarrow \tilde{t}_1 \bar{\tilde{t}}_1$ in fb at $\sqrt{s} = 500$ GeV as a function of $m_{\tilde{t}_1}$ and $\cos \theta_{\tilde{t}}$. ($m_{\tilde{t}_2} = 300$ GeV and $m_{\tilde{g}} = 300$ GeV.)

Fig. 1b: Total cross section of $e^+e^- \rightarrow \tilde{t}_1 \bar{\tilde{t}}_1$ in fb at $\sqrt{s} = 500$ GeV as a function of $\cos \theta_{\tilde{t}}$, for unpolarized (U) as well as left (L) and right (R) polarized e^- beams and $m_{\tilde{t}_1} = 180$ GeV. ($m_{\tilde{t}_2} = 300$ GeV and $m_{\tilde{g}} = 300$ GeV.)

Fig. 2a: Contour lines for the total cross section of $e^+e^- \rightarrow \tilde{t}_2 \bar{\tilde{t}}_2$ in fb at $\sqrt{s} = 2$ TeV as a function of $m_{\tilde{t}_2}$ and $\cos \theta_{\tilde{t}}$. ($m_{\tilde{t}_1} = 300$ GeV and $m_{\tilde{g}} = 700$ GeV.)

Fig. 2b: Total cross section of $e^+e^- \rightarrow \tilde{t}_2 \bar{\tilde{t}}_2$ in fb at $\sqrt{s} = 2$ TeV as a function of $\cos \theta_{\tilde{t}}$, for unpolarized (U) as well as left (L) and right (R) polarized e^- beams and $m_{\tilde{t}_2} = 700$ GeV. ($m_{\tilde{t}_1} = 300$ GeV and $m_{\tilde{g}} = 700$ GeV.)

Fig. 3a: Contour lines for the total cross section of $e^+e^- \rightarrow \tilde{b}_1 \bar{\tilde{b}}_1$ in fb at $\sqrt{s} = 500$ GeV as a function of $m_{\tilde{b}_1}$ and $\cos \theta_{\tilde{b}}$. ($m_{\tilde{b}_2} = 300$ GeV and $m_{\tilde{g}} = 300$ GeV.)

Fig. 3b: Total cross section of $e^+e^- \rightarrow \tilde{b}_1 \bar{\tilde{b}}_1$ in fb at $\sqrt{s} = 500$ GeV as a function of $\cos \theta_{\tilde{b}}$, for unpolarized (U) as well as left (L) and right (R) polarized e^- beams and $m_{\tilde{b}_1} = 180$ GeV. ($m_{\tilde{b}_2} = 300$ GeV and $m_{\tilde{g}} = 300$ GeV.)

Fig. 4a: Contour lines for the total cross section of $e^+e^- \rightarrow \tilde{\tau}_1 \bar{\tilde{\tau}}_1$ in fb at $\sqrt{s} = 500$ GeV as a function of $m_{\tilde{\tau}_1}$ and $\cos \theta_{\tilde{\tau}}$.

Fig. 4b: Total cross section of $e^+e^- \rightarrow \tilde{\tau}_1 \bar{\tilde{\tau}}_1$ in fb at $\sqrt{s} = 500$ GeV as a function of $\cos \theta_{\tilde{\tau}}$, for unpolarized (U) as well as left (L) and right (R) polarized e^- beams and $m_{\tilde{\tau}_1} = 180$ GeV.

Fig. 5: Total cross section of $e^+e^- \rightarrow \tilde{\nu}_\tau \bar{\tilde{\nu}}_\tau$ at $\sqrt{s} = 500$ GeV as a function of $m_{\tilde{\nu}_\tau}$, for unpolarized (U) as well as left (L) and right (R) polarized e^- beams.

Fig. 6: Total cross section of $e^+e^- \rightarrow \tilde{t}_1 \bar{\tilde{t}}_1$ at $m_{\tilde{t}_1} = 180$ GeV and $\cos \theta_{\tilde{t}} = 0.7$ as a function of \sqrt{s} . ($m_{\tilde{t}_2} = 300$ GeV, $m_{\tilde{g}} = 300$ GeV.)

Fig. 7: Gluon, gluino-top, initial state, and total radiative corrections relative to the tree level cross section of $e^+e^- \rightarrow \tilde{t}_1 \bar{\tilde{t}}_1$ at $m_{\tilde{t}_1} = 180$ GeV and $\cos \theta_{\tilde{t}} = 0.7$ as a function of \sqrt{s} . ($m_{\tilde{t}_2} = 300$ GeV, $m_{\tilde{g}} = 300$ GeV.)

Fig. 8a: Kinematically allowed parameter domains in the $M - \mu$ plane for $m_{\tilde{t}_1} = 180$ GeV and $\tan \beta = 2$ for the decays: a) $\tilde{t}_1 \rightarrow c \tilde{\chi}_1^0$, b) $\tilde{t}_1 \rightarrow b W^+ \tilde{\chi}_1^0$, c) $\tilde{t}_1 \rightarrow c \tilde{\chi}_2^0$,

d) $\tilde{t}_1 \rightarrow b \tilde{\chi}_1^+$. e) $\tilde{t}_1 \rightarrow b \tilde{\chi}_2^+$. The grey area is covered by LEP2 for $\sqrt{s} = 190$ GeV.

Fig. 8b: Kinematically allowed parameter domains in the $M - \mu$ plane for $m_{\tilde{b}_1} = 180$ GeV and $\tan \beta = 30$ for the decays: a) $\tilde{b}_1 \rightarrow b \tilde{\chi}_1^0$, b) $\tilde{b}_1 \rightarrow b \tilde{\chi}_2^0$, c) $\tilde{b}_1 \rightarrow b \tilde{\chi}_3^0$. The grey area is covered by LEP2 for $\sqrt{s} = 190$ GeV.

Fig. 9a: Branching ratios for the \tilde{t}_1 decays as a function of M for $m_{\tilde{t}_1} = 180$ GeV, $\cos \theta_{\tilde{t}} = 0.7$, $\tan \beta = 2$, and $\mu = -500$ GeV. The curves correspond to the following transitions: $\circ \tilde{t}_1 \rightarrow c \tilde{\chi}_1^0$, $\blacksquare \tilde{t}_1 \rightarrow b \tilde{\chi}_-^+$, $\star \tilde{t}_1 \rightarrow b W^+ \tilde{\chi}_1^0$. The grey area is covered by LEP2 for $\sqrt{s} = 190$ GeV.

Fig. 9b: Branching ratios for the \tilde{b}_1 decays as a function of M for $m_{\tilde{b}_1} = 180$ GeV, $\cos \theta_{\tilde{b}} = 0.7$, $\tan \beta = 30$, and $\mu = -500$ GeV. The curves correspond to the following transitions: $\circ \tilde{b}_1 \rightarrow b \tilde{\chi}_1^0$, $\square \tilde{b}_1 \rightarrow b \tilde{\chi}_2^0$. The grey area is covered by LEP2 for $\sqrt{s} = 190$ GeV.

Fig. 10a: Branching ratios for the \tilde{b}_1 decays as a function of M for $m_{\tilde{b}_1} = 180$ GeV, $\cos \theta_{\tilde{b}} = 0.7$, $\tan \beta = 30$, and $\mu = -130$ GeV. The curves correspond to the following transitions: $\circ \tilde{b}_1 \rightarrow b \tilde{\chi}_1^0$, $\square \tilde{b}_1 \rightarrow b \tilde{\chi}_2^0$, $\triangle \tilde{b}_1 \rightarrow b \tilde{\chi}_3^0$. The grey area is covered by LEP2 for $\sqrt{s} = 190$ GeV.

Fig. 10b: Branching ratios for the $\tilde{\tau}_1$ decays as a function of M for $m_{\tilde{\tau}_1} = 180$ GeV, $\cos \theta_{\tilde{\tau}} = 0.7$, $\tan \beta = 30$, and $\mu = -130$ GeV. The curves correspond to the following transitions: $\circ \tilde{\tau}_1 \rightarrow \tau \tilde{\chi}_1^0$, $\square \tilde{\tau}_1 \rightarrow \tau \tilde{\chi}_2^0$, $\triangle \tilde{\tau}_1 \rightarrow \tau \tilde{\chi}_3^0$, $\diamond \tilde{\tau}_1 \rightarrow \tau \tilde{\chi}_4^0$, $\blacksquare \tilde{\tau}_1 \rightarrow \nu_\tau \tilde{\chi}_1^-$. The grey area is covered by LEP2 for $\sqrt{s} = 190$ GeV.

Fig. 10c: Branching ratios for the $\tilde{\nu}_\tau$ decays as a function of M for $m_{\tilde{\nu}_\tau} = 180$ GeV, $\tan \beta = 30$, and $\mu = -130$ GeV. The curves correspond to the following transitions: $\circ \tilde{\nu}_\tau \rightarrow \nu_\tau \tilde{\chi}_1^0$, $\square \tilde{\nu}_\tau \rightarrow \nu_\tau \tilde{\chi}_2^0$, $\triangle \tilde{\nu}_\tau \rightarrow \nu_\tau \tilde{\chi}_3^0$, $\diamond \tilde{\nu}_\tau \rightarrow \nu_\tau \tilde{\chi}_4^0$, $\blacksquare \tilde{\nu}_\tau \rightarrow \tau \tilde{\chi}_1^+$. The grey area is covered by LEP2 for $\sqrt{s} = 190$ GeV.

Fig. 11: Branching ratio for the decays of the heavier stop as a function of M for $\tan \beta = 2$ and $\mu = -1$ TeV.

(a) shows the decays into fermions: $\text{---} \tilde{t}_2 \rightarrow t \tilde{g}$, $\circ \tilde{t}_2 \rightarrow t \tilde{\chi}_1^0$, $\square \tilde{t}_2 \rightarrow t \tilde{\chi}_2^0$, $\blacksquare \tilde{t}_2 \rightarrow b \tilde{\chi}_1^+$. (b) shows the decays into bosons: $\circ \tilde{t}_2 \rightarrow Z \tilde{t}_1$, $\square \tilde{t}_2 \rightarrow h^0 \tilde{t}_1$, $\triangle \tilde{t}_2 \rightarrow H^0 \tilde{t}_1$, $\diamond \tilde{t}_2 \rightarrow A^0 \tilde{t}_1$, $\blacksquare \tilde{t}_2 \rightarrow W^+ \tilde{b}_1$. The grey area is covered by LEP2 for $\sqrt{s} = 190$ GeV.

Fig. 12: Branching ratio for the decays of the heavier sbottom as a function of M for $\tan \beta = 30$ and $\mu = -1$ TeV.

(a) shows the decays into fermions: $\text{---} \tilde{b}_2 \rightarrow b \tilde{g}$, $\circ \tilde{b}_2 \rightarrow b \tilde{\chi}_1^0$, $\square \tilde{b}_2 \rightarrow b \tilde{\chi}_2^0$, $\blacksquare \tilde{b}_2 \rightarrow t \tilde{\chi}_1^-$. (b) shows the decays into bosons: $\circ \tilde{b}_2 \rightarrow Z \tilde{b}_1$, $\square \tilde{b}_2 \rightarrow h^0 \tilde{b}_1$, $\triangle \tilde{b}_2 \rightarrow H^0 \tilde{b}_1$.

$\diamond \tilde{b}_2 \rightarrow A^0 \tilde{b}_1$, $\blacksquare \tilde{b}_2 \rightarrow W^- \tilde{t}_1$, $\bullet \tilde{b}_2 \rightarrow H^- \tilde{t}_1$. The grey area is covered by LEP2 for $\sqrt{s} = 190$ GeV.

Fig. 13: Branching ratio for the decays of the heavier stau as a function of M for $\tan\beta = 30$ and $\mu = -1$ TeV.

(a) shows the decays into fermions: $\circ \tilde{\tau}_2 \rightarrow \tau \tilde{\chi}_1^0$, $\square \tilde{\tau}_2 \rightarrow \tau \tilde{\chi}_2^0$, $\blacksquare \tilde{\tau}_2 \rightarrow \nu_\tau \tilde{\chi}_1^-$.
(b) shows the decays into bosons: $\circ \tilde{\tau}_2 \rightarrow Z \tilde{\tau}_1$, $\square \tilde{\tau}_2 \rightarrow h^0 \tilde{\tau}_1$, $\triangle \tilde{\tau}_2 \rightarrow H^0 \tilde{\tau}_1$, $\diamond \tilde{\tau}_2 \rightarrow A^0 \tilde{\tau}_1$. The grey area is covered by LEP2 for $\sqrt{s} = 190$ GeV.

Fig. 14: Branching ratio for the decays of the tau sneutrino as a function of M for $\tan\beta = 30$ and $\mu = -1$ TeV.

(a) shows the decays into fermions: $\circ \tilde{\nu}_\tau \rightarrow \nu_\tau \tilde{\chi}_1^0$, $\square \tilde{\nu}_\tau \rightarrow \nu_\tau \tilde{\chi}_2^0$, $\blacksquare \tilde{\nu}_\tau \rightarrow \tau \tilde{\chi}_1^+$.
(b) shows the decays into bosons: $\blacksquare \tilde{\nu}_\tau \rightarrow W^+ \tilde{\tau}_1$, $\bullet \tilde{\nu}_\tau \rightarrow H^+ \tilde{\tau}_1$. The grey area is covered by LEP2 for $\sqrt{s} = 190$ GeV.

Fig. 15: Background reactions and their cross sections for $\sqrt{s} = 500$ GeV.

Fig. 16: $E_{vis}/\sqrt{s} < 0.4$ for $\tilde{\chi}_1^0 c \tilde{\chi}_1^0 \bar{c}$, qq, WW, eW ν , tt, ZZ, eeZ.

Fig. 17: $m_{inv} > 120$ GeV for $\tilde{\chi}_1^0 c \tilde{\chi}_1^0 \bar{c}$, qq, WW, eW ν , tt, ZZ, eeZ.

Fig. 18: Sensitivity for an $e^+e^- \rightarrow \tilde{t}_1 \tilde{t}_1^* \rightarrow \tilde{\chi}_1^0 c \tilde{\chi}_1^0 \bar{c}$ signal. Open histograms show the simulated signal, solid and hatched histograms show the remaining background after all selection cuts are applied.

Fig. 19: Thrust < 0.85 for $\tilde{\chi}_1^+ b \tilde{\chi}_1^- \bar{b}$, qq, WW, eW ν , tt, ZZ, eeZ.

Fig. 20: Number of cluster ≥ 60 for $\tilde{\chi}_1^+ b \tilde{\chi}_1^- \bar{b}$, qq, WW, eW ν , tt, ZZ, eeZ.

Fig. 21: Sensitivity for an $e^+e^- \rightarrow \tilde{t}_1 \tilde{t}_1^* \rightarrow \tilde{\chi}_1^+ b \tilde{\chi}_1^- \bar{b}$ signal. Open histograms show the simulated signal, solid and hatched histograms show the remaining background after all selection cuts are applied.

Fig. 22: Detection confidence levels. (a) $\tilde{\chi}_1^+ b \tilde{\chi}_1^- \bar{b}$ channel. (b) $\tilde{\chi}_1^0 c \tilde{\chi}_1^0 \bar{c}$ channel.

Fig. 23: Discovery region for $\sqrt{s} = 500$ GeV and $\mathcal{L} = 50 \text{ fb}^{-1}$. In the shaded area a 3σ effect is expected.

Fig. 24: Discovery region for $\sqrt{s} = 800$ GeV and $\mathcal{L} = 200 \text{ fb}^{-1}$. In the shaded area a 3σ effect is expected.

Fig. 25: Error bands for the total tree-level cross section of $e^+e^- \rightarrow \tilde{t}_1 \tilde{t}_1^*$ in fb

at $\sqrt{s} = 400$ GeV and $\sqrt{s} = 500$ GeV as a function of $m_{\tilde{t}_1}$ and $\cos\theta_{\tilde{t}}$. The dot corresponds to $m_{\tilde{t}_1} = 180$ GeV and $\cos\theta_{\tilde{t}} = 0.57$. The error bands are defined by $(\sigma_{400}, \Delta\sigma_{400}) = (18.2, 4.1)$ fb and $(\sigma_{500}, \Delta\sigma_{500}) = (47.4, 5.5)$ fb.

Fig. 26: Error bands (dashed) and the corresponding error ellipse as a function of $m_{\tilde{t}_1}$ and $\cos\theta_{\tilde{t}}$ for the total tree-level cross sections of $e^+e^- \rightarrow \tilde{t}_1\tilde{t}_1$ in fb at $\sqrt{s} = 500$ GeV with 90% left- and right-polarized electron beam. The dot corresponds to $m_{\tilde{t}_1} = 180$ GeV and $\cos\theta_{\tilde{t}} = 0.57$. The error bands are defined by $(\sigma_L, \Delta\sigma_L) = (48.6, 6.0)$ fb and $(\sigma_R, \Delta\sigma_R) = (46.1, 4.9)$ fb.

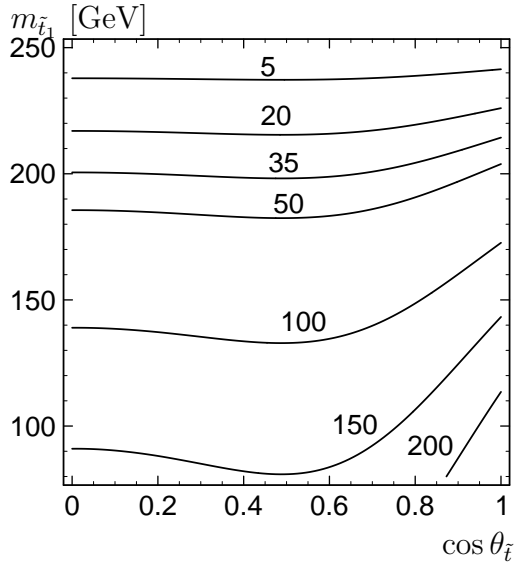


Fig. 1a

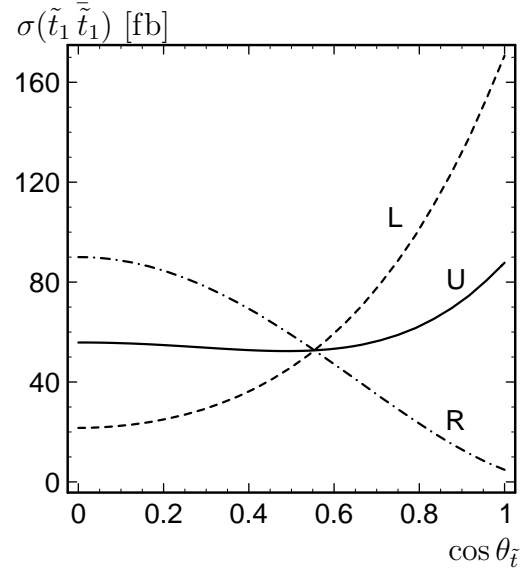


Fig. 1b

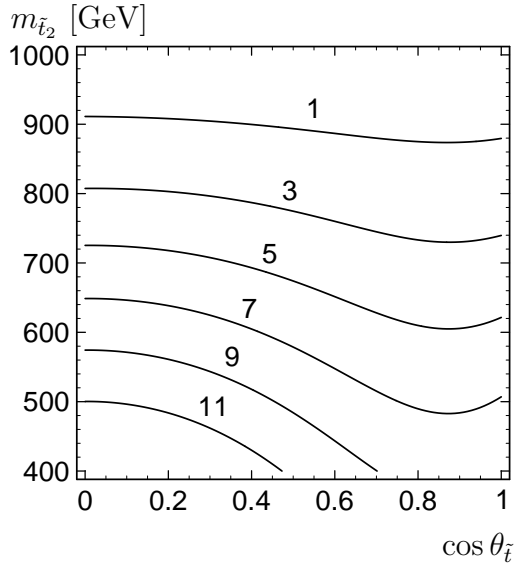


Fig. 2a

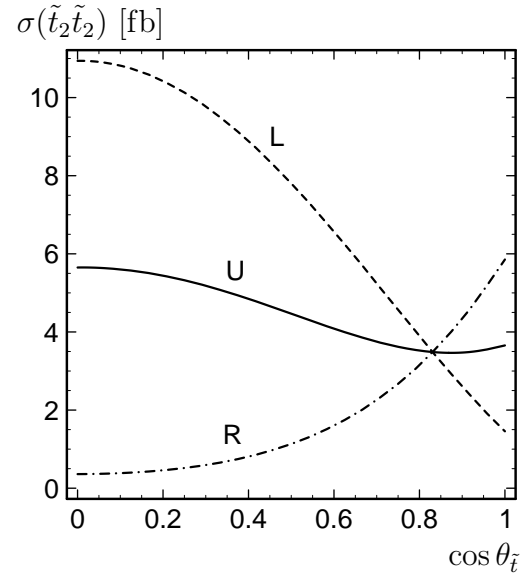


Fig. 2b

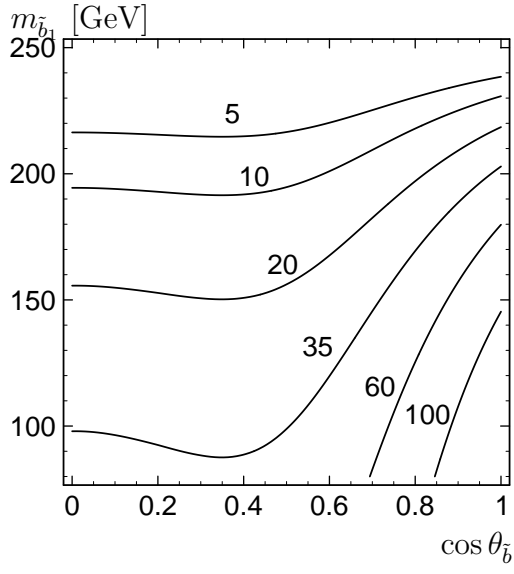


Fig. 3a

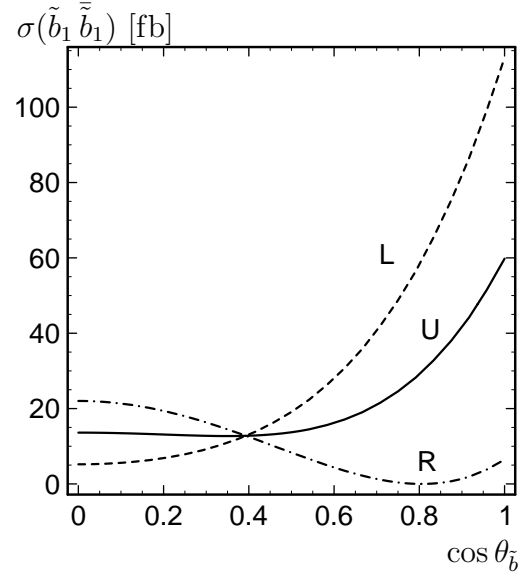


Fig. 3b

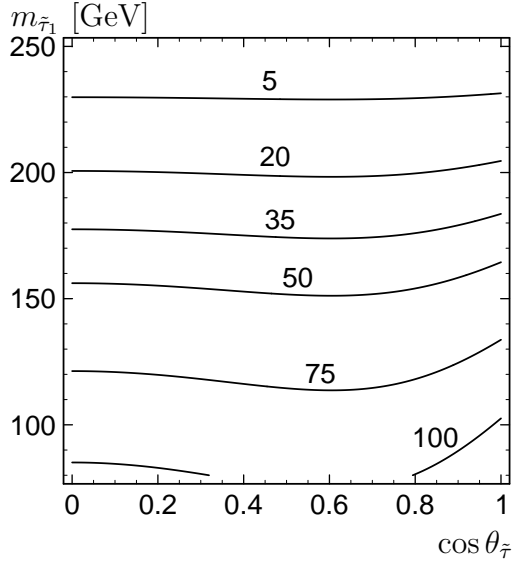


Fig. 4a

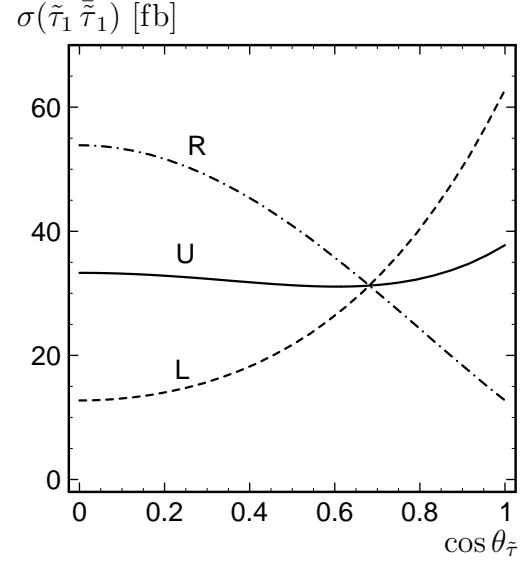


Fig. 4b

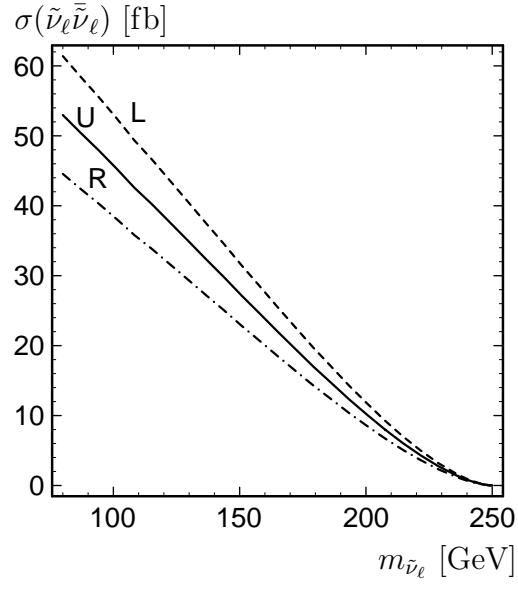


Fig. 5

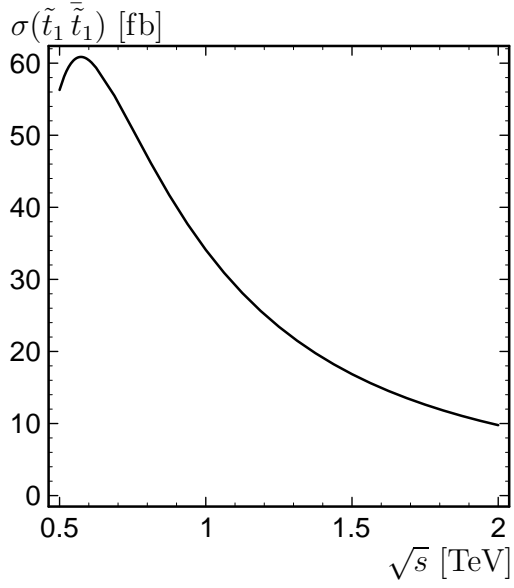


Fig. 6

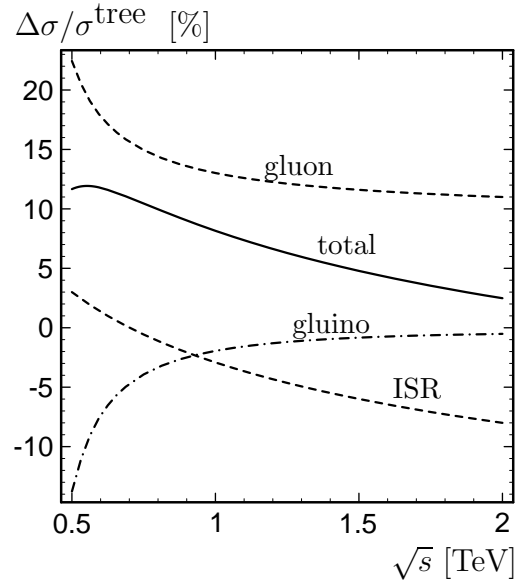


Fig. 7

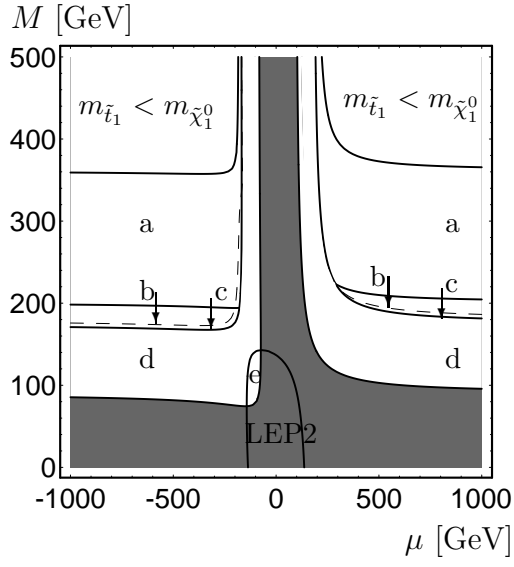


Fig. 8a

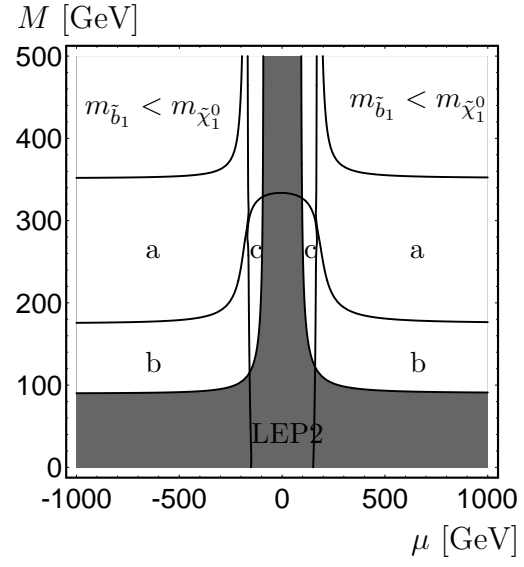


Fig. 8b

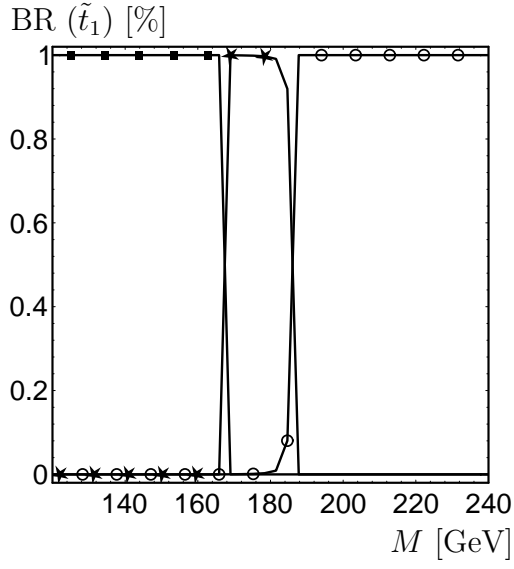


Fig. 9a

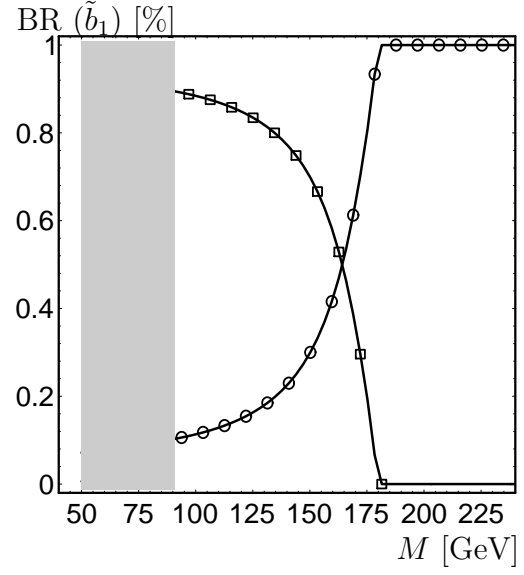


Fig. 9b

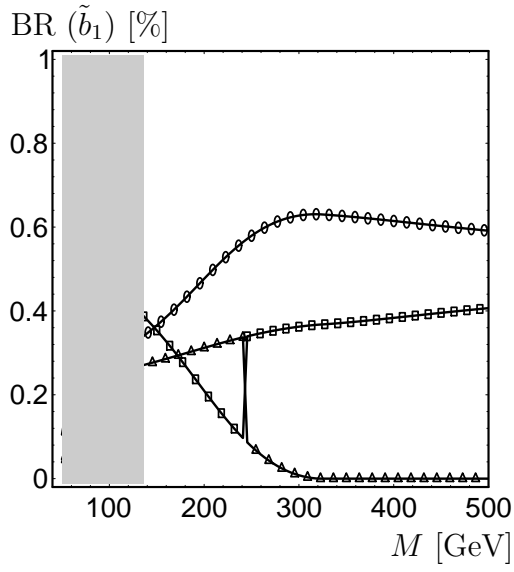


Fig. 10a

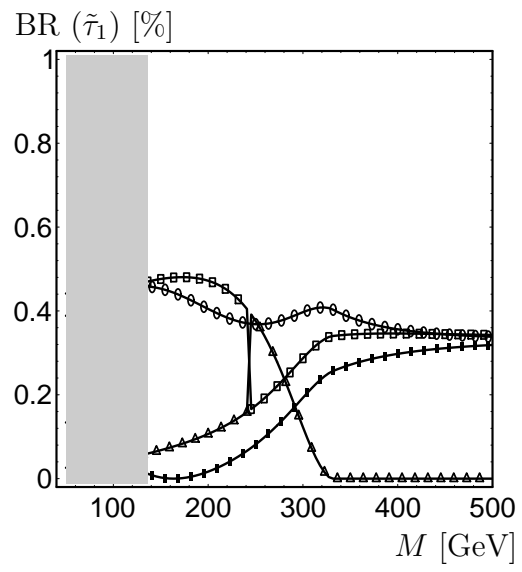


Fig. 10b

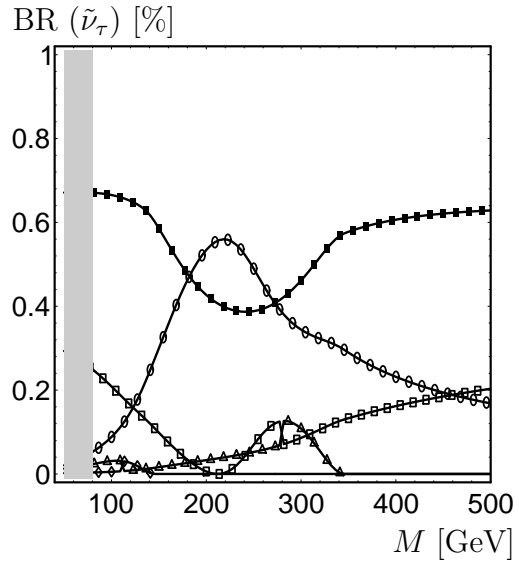


Fig. 10c

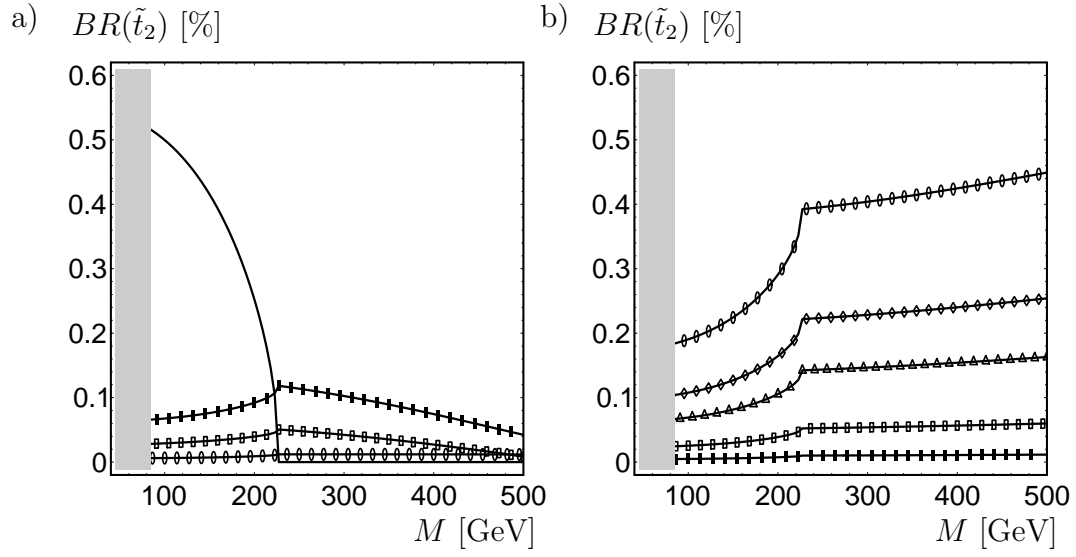


Fig. 11

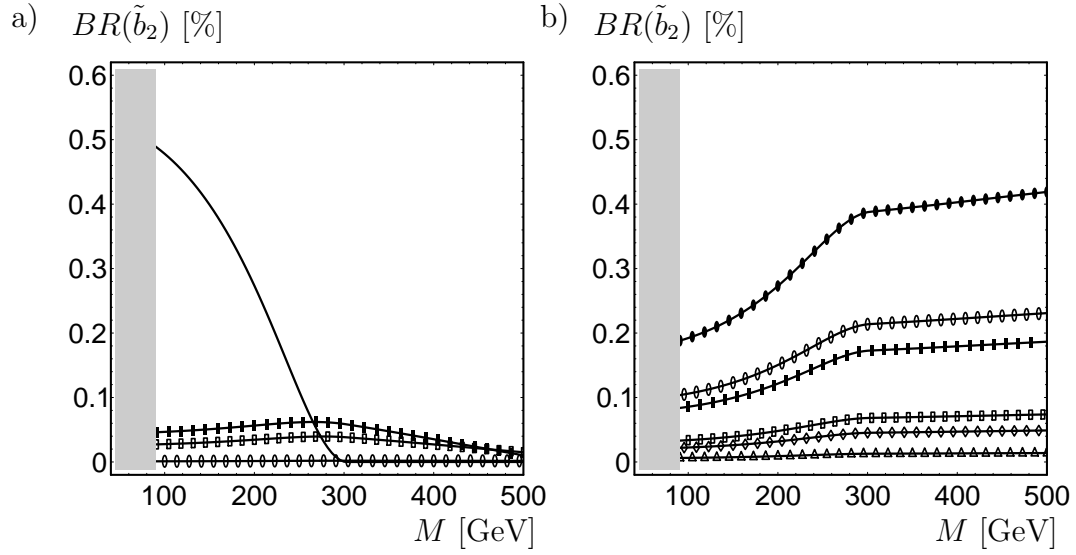


Fig. 12

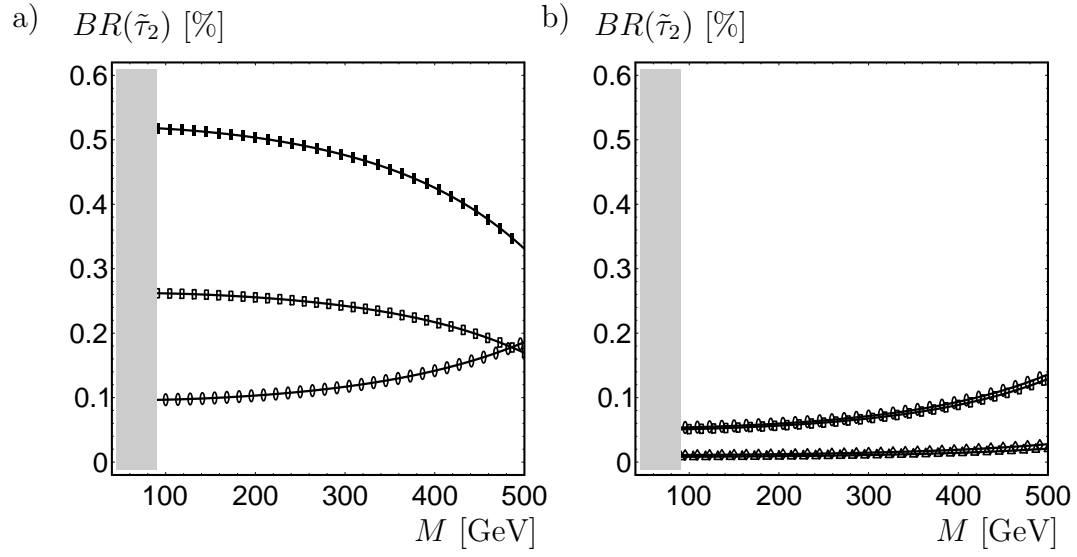


Fig. 13

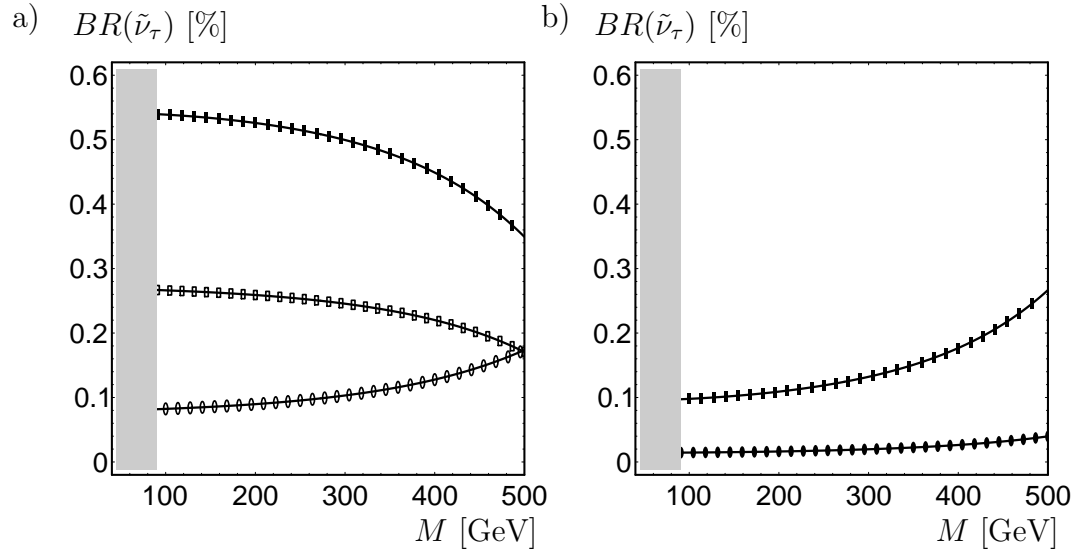


Fig. 14

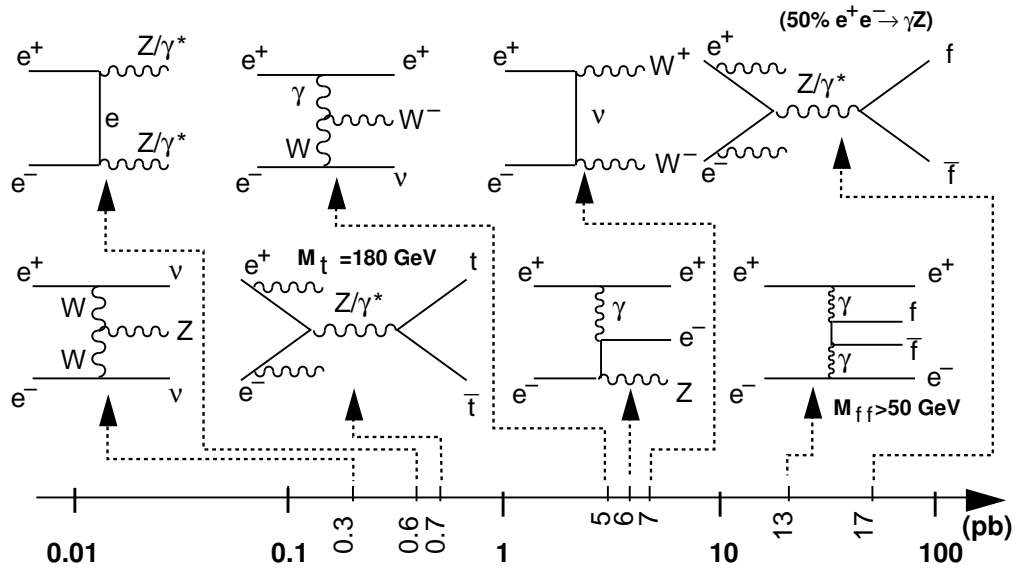


Fig. 15

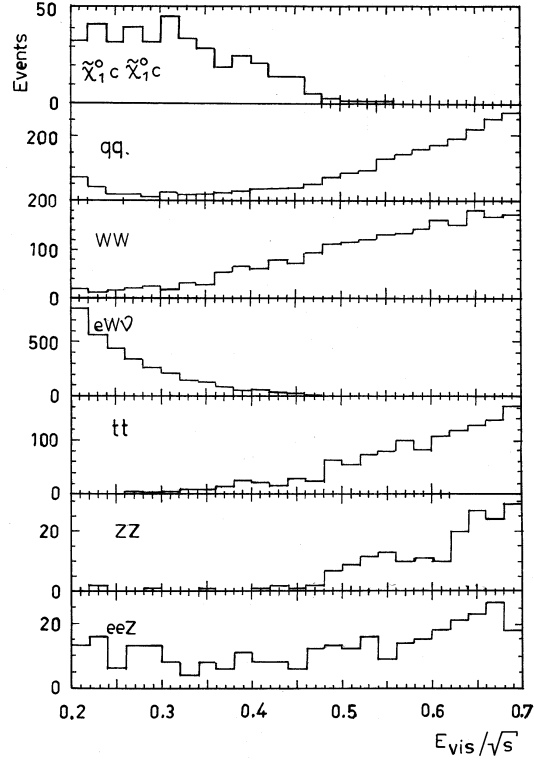


Fig. 16

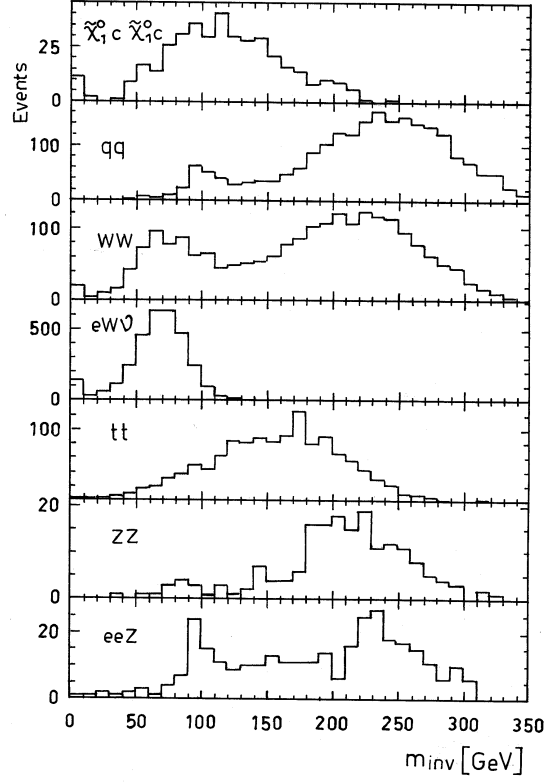


Fig. 17

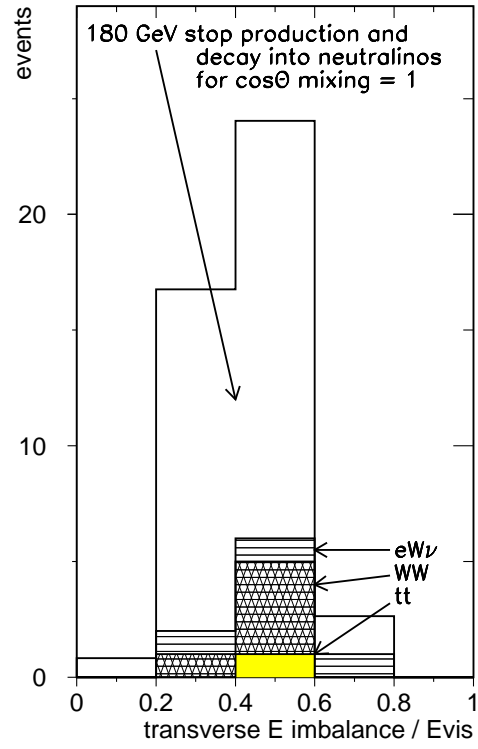


Fig. 18

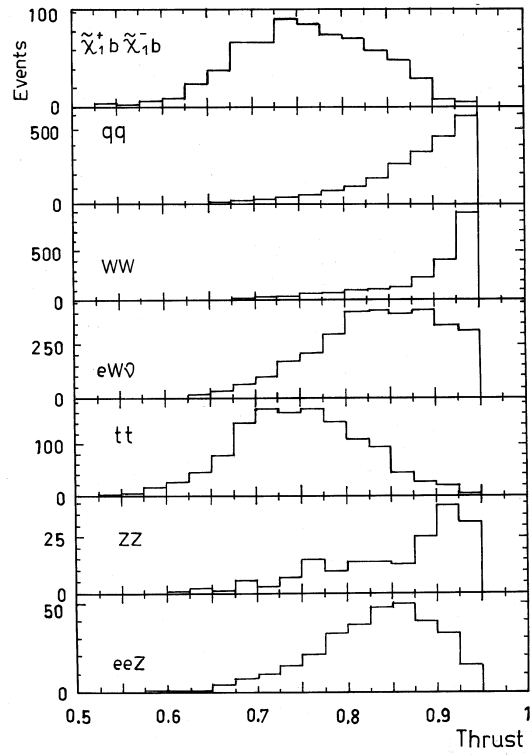


Fig. 19

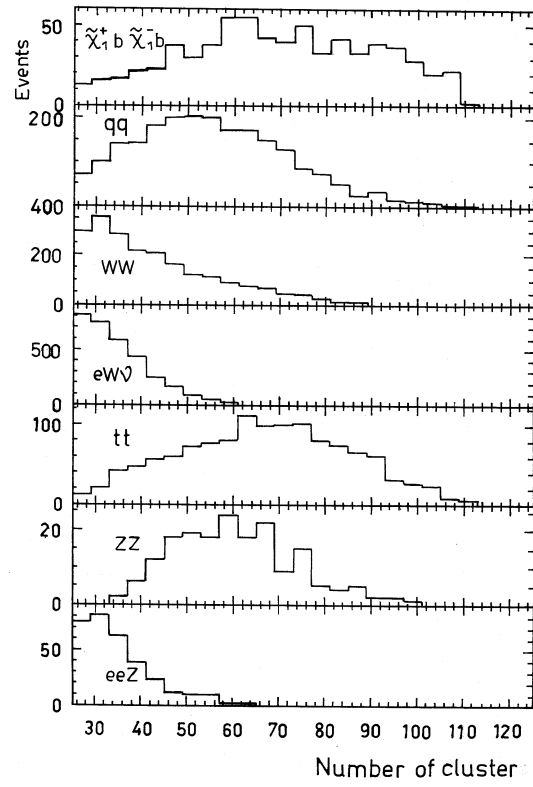


Fig. 20

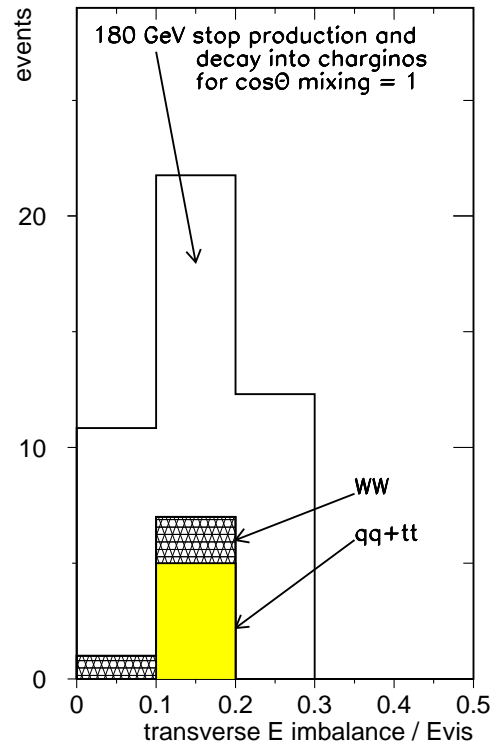


Fig. 21

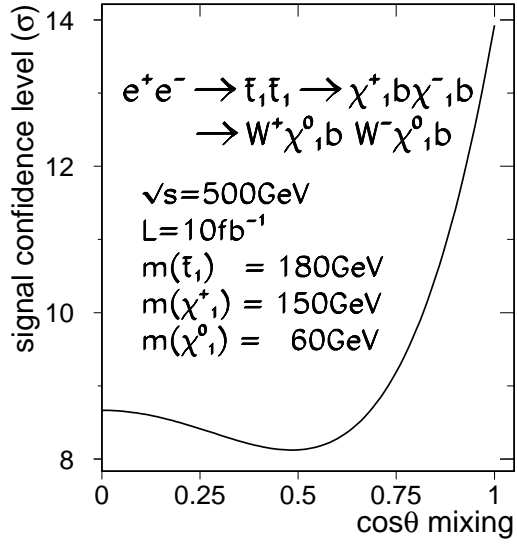


Fig. 22a

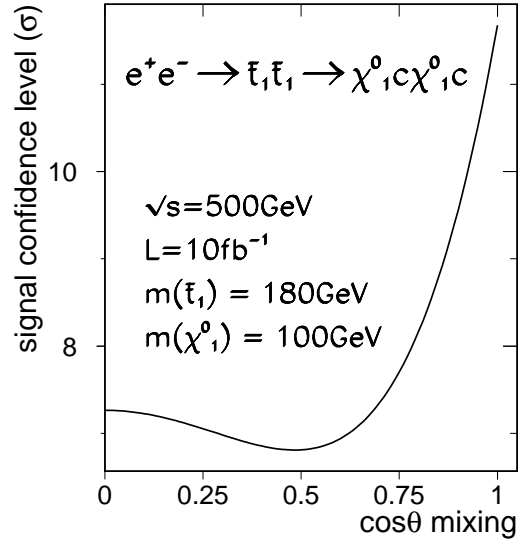


Fig. 22b

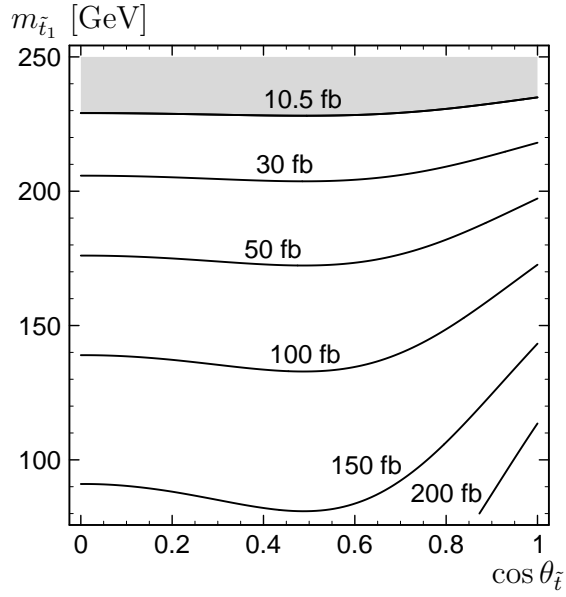


Fig. 23

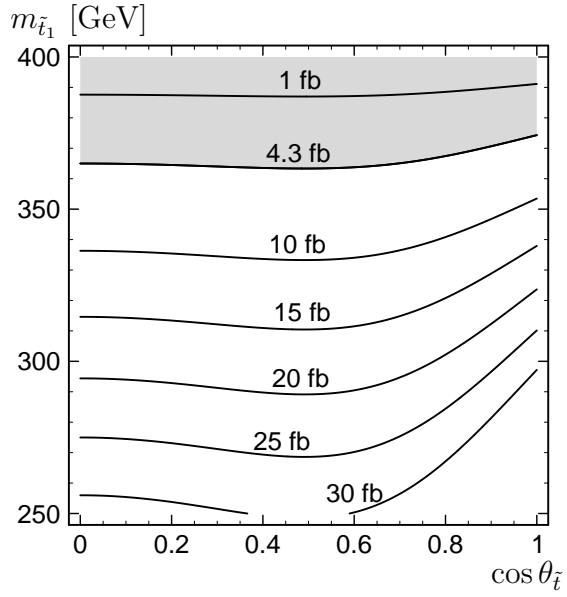


Fig. 24

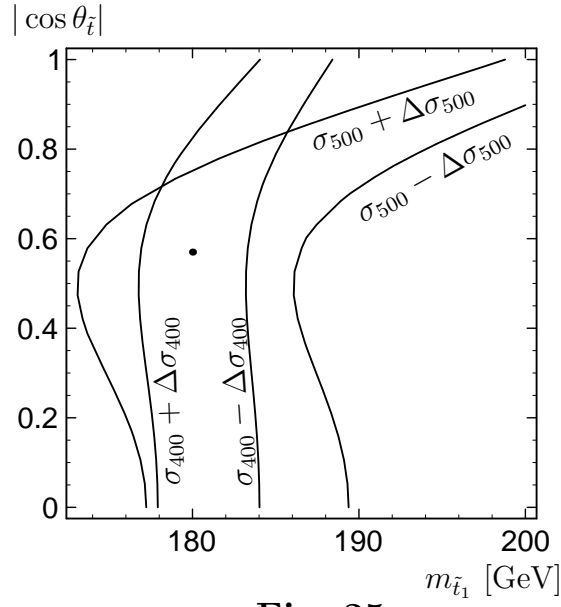


Fig. 25

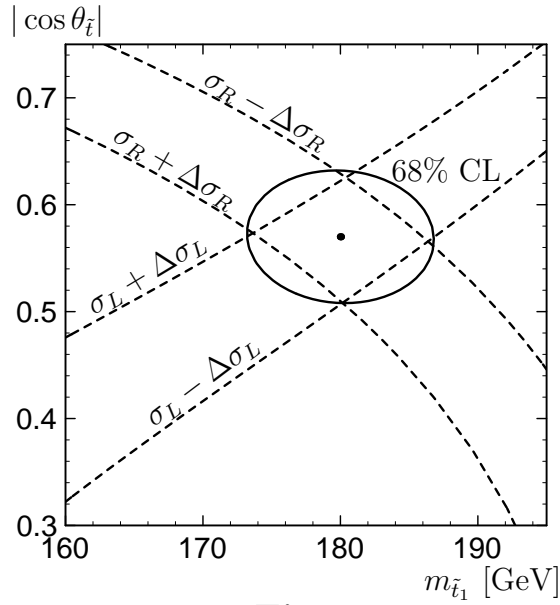


Fig. 26

